ADVANCED ENERGY MATERIALS
www.advenergymat.de

Understanding the Metal-Center Mediated Adsorption and Redox Mechanisms in a $FeMn(NbTa)_2O_6$ Columbite Material for Anion Exchange Membrane Water Electrolyzers

Patrick M. Bacirhonde, Devendra Shrestha, Kyoungin Kang, Esensil Man Hia, Nikhil Komalla, Nelson Y. Dzade, Merve Buldu-Akturk, Michelle P. Browne, Milan Babu Poudel, Dong Jin Yoo, Eun-Suk Jeong, Ahmed Yousef Mohamed, Byoung Gun Han, Deok-Yong Cho,* Matthew T. Curnan, Geun Ho Gu, Jeong Woo Han, and Chan Hee Park**

The rising demand for sustainable green hydrogen production necessitates efficient and cost-effective water-splitting electrocatalysts. Inspired by the catalytic activities of columbite-tantalite, this study combines a scalable cutting-edge synthesis approach with atomic-level structures and metal-center-mediated mechanisms to unravel its operational performance and stability. Using ad in situ X-ray absorption fine structure combined with Density Functional Theory (DFT), the results reveal distinctive valence band peaks and moderate charge transfer from Mn and Fe sites, enabling stable adsorption and reduced activation barriers. In contrast, the high-valence Nb and Ta centers at the B-sites promote favorable *d*-band alignment, enhancing orbital overlap with oxygen *p*-orbitals. This facilites electronic delocalization, lowers charge accumulation, and reduces activation barriers of intermediates species. Fe and Mn at the A-sites exhibit strong redox reactivity and optimal adsorption for OH* and O*, supporting efficient electron fransfers. Solvation effects modeled via VASPsol further stabilize key intermediates, especially O*, reducing the energy barrier for water dissociation. Notably, $FeMn(NbTa)_2O_6$-columbite catalysts stand out with a cell voltage of 1.81 V at a current density of 700 mA cm^{-2}, compared to 40% Pt/C-RuO_2 (1.75 V) at the same current density in the anion exchange membrane water electrolyzer (AEMWE). Also, the $FeMn(NbTa)_2O_6$-columbite exhibits long-term stability at 800 mA cm^{-2}, surpassing the benchmark 40% Pt Vulcan-RuO_2 after 200 h in AEMWE. This work significantly advances current research and establishes a design rule for selecting metal compositions in the development of advanced electrocatalysts in alkaline water electrolyzers.

1. Introduction

Electrochemical water-splitting offers a low-cost feasible approach for the scalable production of sustainable green hydrogen, which has a significant opportunity to replace traditional fossil fuels, mitigating energy and environmental concerns.[1] Nevertheless, both the cathodic HER and anodic OER processes are kinetically slow, requiring the introduction of highly active electrocatalysts to accelerate reaction kinetics and overcome threshold energy barriers. Currently, the platinum group material and NiFeOOH-based materials are the benchmark catalysts for HER or OER, but their scarcity and prohibitive prices hugely impede large-scale industrialization. The design of noble metal-free large-scale electrocatalysts for water-splitting with high activity and good durability is still challenging.[2] Therefore, the design of noble metal-free, large-scale electrocatalysts for water-splitting with high activity and good durability remains a significant challenge. An effective approach to enhance overall water-splitting

P. M. Bacirhonde, D. Shrestha, K. Kang, E. M. Hia, C. H. Park
Department of Bionanotechnology and BionanoConvergence Engineering
Graduate School
Jeonbuk National University
Jeonju 54896, Republic of Korea
E-mail: biochan@jbnu.ac.kr
The ORCID identification number(s) for the author(s) of this article can be found under https://doi.org/10.1002/aenm.202404479

DOI: 10.1002/aenm.202404479

P. M. Bacirhonde
Regional Leading Research Center for Nanocarbon-based Energy Materials and Application Technology
Jeonbuk National University
Jeonju 54896, South Korea

N. Komalla, N. Y. Dzade
Department of Energy and Mineral Engineering
Pennsylvania State University
University Park, PA 16802, USA
E-mail: nxd5313@psu.edu

M. Buldu-Akturk, M. P. Browne
Helmholtz Young Investigator Group Electrocatalysis: Synthesis to Devices
Helmholtz-Zentrum Berlin für Materialien und Energie
12489 Berlin, Germany

efficiency is to engineer electrocatalysts with controlled interstitial defects, which can lower activation energies and modulate the electronic structure of active sites. Unlike general defect tolerance, which may imply a passive acceptance of defects, the deliberate introduction and control of interstitial defects have shown to be pivotal in improving oxygen evolution reaction (OER) performance. For example, a study on Fe-doped NiO catalysts demonstrated that oxygen vacancies enhance OER performance by increasing active site density and stabilizing intermediates such as OH* and O*, thereby improving charge transfer dynamics and surpassing benchmark IrO_2 activity.[3] Zhou et al. emphasized the role of octahedral unit engineering in spinel oxides to enhance OER performance. Controlled interstitial defects, such as oxygen vacancies, were introduced to adjust the cation distribution in octahedral units, which are critical for catalytic activity. The study found that octahedral sites with redox-active cations (for example, Co^{3+}) exhibited strong metal-oxygen covalency and efficient orbital overlap, facilitating intermediate adsorption and charge transfer.[4] Wang et al. demonstrates that a dynamically adjustable geometry can optimize both metal and oxygen redox activities by introducing asymmetry in the NiO_6 structure, via strain engineering or vacancies increases orbital energy splitting. This results in a non-overlapping region between d_{z^2} and anti-bonding states, enabling efficient electron transfer.[5] Also, some strategies have been employed, such as adding metallic dopants to Ni-Fe-*X* or Fe-Co-*X* systems with high valence charges (X = Nb, Ta, W, Re), modulating 3*d* metals (Fe, Mn, Co) toward lower energies and furthering valence charge transitions to enhance catalytic performance.[6] A previous work demonstrated that the incorporation of high-valance Ta can stabilize otherwise unstable low Fe^{2+} charges.[7] The orthorhombic columbite-tantalite with chemical composition $FeMn(NbTa)_2O_6$, has been investigated for various applications. These include capacitors due to robust columbite-tantalite stability, high surface area, and intrinsic properties related to bandgap and high dielectric constant.[8] The energy required to drive the catalytic reaction at the cathode and anode is greatly affected by the bandgap energy and the electric field generated by the catalyst. The local electric field around Fe atoms, created by the distorted FeO_6 octahedra due to the Jahn-Teller effect, is supposed to enhance the catalytic activity of HER and OER.[9]

In our previous work, we developed reduced $Fe_{0.79}Mn_{0.21}Nb_{0.16}Ta_{0.84}O_6$ columbite-tantalite with 2D nanostructures as highly efficient electrocatalysts for water-splitting.[9] They benefit from having unsaturated edge atom coordination at their active sites, namely for the adsorption and catalytic conversion of water molecules to free hydrogen and oxygen gases.[9,10] However, further experimental and computational studies indicate that the catalytic active sites are almost entirely absent on the inert basal planes of transition metal oxides. Simultaneously, poor electron transport exists between catalysts and adsorbed molecules, which extremely limits the practical application of columbites for green energy production. To solve these problems, many techniques have been developed, such as phase engineering,[11] interface electronic coupling, and doping engineering.[12] In addition, the processing condition can also affect the defect density and concentration of oxygen vacancies, which modulates the electronic properties.[13] Considering the ultimate goal of catalyst development is to have enough knowledge of the factors determining catalytic activity to be able to tailor catalysts atom-by-atom, doping engineering has become an attractive strategy to modify the electronic structure of columbite-tantalite and increase its intrinsic electrical conductivity, which is required for increased electrocatalyst activity. Fe/Mn at the A-sites and Ta/Nb atoms at the B-sites of AB_2O_6-columbites have different electronegativities, which may lead to quick charge transfer and thereby modification of the electronic properties of materials.[9,14] Zheng et al. underlined the role of structural defects, such as oxygen vacancies, in enhancing OER performance by facilitating charge transfer and improving metal-oxygen covalency, emphasizing the importance of local structural asymmetry.[15] Similarly, Wang et al. demonstrated how cation engineering can tailor electronic configurations, where doping enhances conductivity and optimizes catalytic performance.[16] Additionally, Ruiz-Cornejo et al. showcased

M. B. Poudel, D. J. Yoo
Department of Energy Storage/Conversion Engineering (BK21 FOUR) of Graduate School
Hydrogen and Fuel Cell Research Center
Jeonbuk National University
567 Baekje-daero, Deokjin-gu, Jeonju-si, Jeollabuk-do 54896, Republic of Korea

E.-S. Jeong
Division of Science Education and Institute of Fusion Science
Jeonbuk National University
Jeonju, Jeonbuk 54896, Republic of Korea

A. Y. Mohamed, B. G. Han, D.-Y. Cho
Department of Physics
Jeonbuk National University
Jeonju 54896, Republic of Korea
E-mail: zax@jbnu.ac.kr

M. T. Curnan, G. H. Gu
Institute for Hydrogen Energy
Korea Institute of Energy Technology (KENTECH)
200 Hyeoksin-ro, Naju 58330, Republic of Korea

J. W. Han
Department of Materials Science and Engineering
Research Institute of Advanced Materials
Seoul National University
1 Gwanak-ro, Gwanak-gu, Seoul 08826, Republic of Korea

C. H. Park
Division of Mechanical Design Engineering
Graduate School
Jeonbuk National University
Jeonju 54896, Republic of Korea

C. H. Park
Department of Bionanosystem Engineering
Graduate School
Jeonbuk National University
Jeonju 54896, Republic of Korea

C. H. Park
Eco-friendly Machine Parts Design Research Center
Jeonbuk National University
Jeonju, Republic of Korea

C. H. Park
Interventional Mechano-Biotechnology Convergence Research Center
Jeonbuk National University
Jeonju, Republic of Korea

C. H. Park
Innovative Mechanobio Active Materials Based Medical Device Demonstration Center
Jeonbuk National University
Jeonju, Republic of Korea

the impact of synthesis techniques, including transition metal doping, on structural and electronic properties, revealing how controlled processing significantly influences OER efficiency.[17] These findings underscore the importance of developing quantitative structure-property-activity relationships to correlate catalytic activities with the structural and electronic attributes of AB_2O_6-columbite, which remains a critical challenge. In addition to atomic structure, the synthesis and processing of AB_2O_6-columbite also play pivotal roles in shaping its properties as both a dielectric material and an electrocatalyst, enabling effective catalysis of water splitting into its constituent elements.[18] Herein, we successfully synthesized AB_2O_6-columbite families ($FeNb_2O_6$ (FNO), $FeTa_2O_6$ (FTO) $MnNb_2O_6$ (MNO), $MnTa_2O_6$ (MTO), and $FeMn(NbTa)_2O_6$ (TNO)) with controlled defects via facile hydrothermal synthesis and a controlled thermal treatment. Compared to the Ni benchmark, we found that $FeMn(NbTa)_2O_6$-columbite exhibits outstanding OER activity in alkaline media. Water electrolyzer technologies are generally classified into proton exchange membrane (PEM) electrolysis, alkaline liquid electrolysis, anion exchange membrane (AEM) electrolysis, and solid oxide electrolysis cells (SOECs). PEM operates in acidic environments (pH≈0); AEM electrolyzers combine the benefits of PEM and alkaline systems, utilizing a solid polymer membrane and operating under alkaline conditions (pH ≈14) at temperatures of 50–80 °C, applying a typical cell voltage of 1.8–2.2 V. The SOECs function at high temperatures (700–900 °C) using ceramic electrolytes, enabling high efficiency through thermal energy integration. These differences necessitate distinct materials and catalyst design strategies. Among them, AEM is particularly attractive due to its compatibility with earth-abundant catalysts, lower cost, and better long-term stability, making it ideal for scalable green hydrogen production. Furthermore, the $FeMn(NbTa)_2O_6$-columbite performance in an anion exchange membrane water electrolyzer (AEMWE) assembly was assessed and achieved a cell voltage of 1.81 V at 700 mA cm^{-2}. $FeMn(NbTa)_2O_6$ further demonstrated durability after 200 h and maintained a cell voltage of about 1.85 V. The rationale for the OER performance of the $FeMn(NbTa)_2O_6$ material was investigated by employing in situ x-ray absorption fine structure and density functional theory (DFT) calculations to predict the active sites and adsorption energies of intermediates, identifying the most energetically favorable paths for water dissociation.

2. Results and Discussion

2.1. AB_2O_6 Columbite Preparation and Characterization

The AB_2O_6 nanoparticles of $FeNb_2O_6$, $FeTa_2O_6$, $MnNb_2O_6$, $MnTa_2O_6$, and $FeMn(NbTa)_2O_6$-columbite were prepared in A/2B ratios. Briefly, a series of AB_2O_6-columbite nanoparticles were first synthesized via a conventional sol-gel crystallization of homogeneously cross-linked metal cations, followed by hydrothermal treatment of the colloidal solution, as illustrated in **Figure 1a**. Metal cation precursors, such as Fe and Ta, were combined in a stoichiometric ratio to achieve the desired A:B cation composition and then homogeneously mixed through sonication, followed by vigorous stirring. The resulting colloidal solution was transferred into a Teflon-lined stainless-steel autoclave and subjected to hydrothermal treatment. The hydrothermal nanoparticles were further lyophilized to reduce physical instability, namely by cross-linking homogeneously distributed metal cations.[19] The amorphous particles obtained at 110 °C ($FeMn(NbTa)_2O_6$-110), which are not well crystallized (Figure S1, Supporting Information), were then annealed at 1200 °C under H_2/Ar atmosphere ($FeMn(NbTa)_2O_6$-1200) to increase their crystallinity as shown in Figure 1b and Figure S2, Supporting Information, introducing interstitial lattice defects within them.[20] The $FeNb_2O_6$, $FeTa_2O_6$, $MnNb_2O_6$, $MnTa_2O_6$, and $FeMn(NbTa)_2O_6$ phases crystallized in the orthorhombic *Pbcn* space group (a = 5.136, b = 5.878, c = 14.557, α = 90.0, β = 90.0, γ = 90.0; unit-cell volume = 439.48 Å^3), as shown in Figure 1c. The high-resolution powder diffraction (HRPD) pattern of $FeMn(NbTa)_2O_6$ exhibited four distinct peak families (Figure S3, Supporting Information) corresponding to Fe_2O_3 (JCPDS card: #96-400-2384),[21] MnO (JCPDS card: #96-154-1154),[22] Ta_2O_5 (JCPDS card: #96-153-3574),[23] and Nb_2O_5 (JCPDS card: #00-027-1312).[24] The crystal structures and atomic arrangements of the $FeNb_2O_6$, $FeTa_2O_6$, $MnNb_2O_6$, $MnTa_2O_6$, and $FeMn(NbTa)_2O_6$ phases in their layered Columbite-tantalite configurations are illustrated in Figure S4, Supporting Information. The bond distances in Figure S5, Supporting Information, range from 2.11 to 2.27 Å for Fe-O, 2.11 to 2.27 Å for Mn-O, 1.81 to 2.19 Å for Nb-O, and 1.87 to 2.16 Å for Ta-O. As illustrated in Figure S6, Supporting Information, the specific surface area of $FeMn(NbTa)_2O_6$-1200 after N_2 gas adsorption is 1082×10^{-4} m^2 g^{-1}, the pore volume is 194×10^{-6} cm^3 g^{-1}, and the average pore diameter is 71.8 Å.

The Raman spectra of $FeMn(NbTa)_2O_6$ and $MnNb_2O_6$ (Figure S7, Supporting Information) are compared to distinguish their vibrational modes, providing insights into their structural properties. The observed modes of vibrations can be grouped into three general families of lattice vibrations. First, we observe the translation of *A*-site cations occurs at frequencies below 150 cm^{-1}. These vibrations correspond to the translational motions of A-site Fe^{2+} or Mn^{2+} ions within the crystal lattices of FeO_6 or MnO_6 octahedra. They provide valuable information about the movement and arrangement of the metal ions and octahedral units in the material. Second, we observed the Fe-Mn-O or Mn-Nb-O stretching vibrations occur within the range of 150 to 550 cm^{-1}. These vibrations arise from the bending modes of the chemical bonds between oxygen (O) atoms and (Fe-Nb, Mn-Nb) or (Fe-Ta, Mn-Ta) atom pairs. They offer insights into the structural characteristics and connectivity of the Fe-Mn-Ta-Nb-O octahedra, including bond angles and distortions. We observe that $MnNb_2O_6$ samples show a clear distinction between the A and B sites, in contrast with those of $FeMn(NbTa)_2O_6$, indicating the absence of dual cations at each site. Last, the Nb-O or Ta-O stretching modes occurring at a frequency of 868 cm^{-1}, result from the stretching motions of the chemical bonds between Ta-O or Nb-O within the Ta/NbO_6 octahedra framework. They reflect the strength and nature of Ta-O/Nb-O chemical bonds, as well as the symmetries of TaO_6/NbO_6 octahedra.

Atomic force microscopy (AFM) images shown in Figure S8, Supporting Information reveal that the average grain size decreased in $FeNb_2O_6$ while increasing in $FeMn(NbTa)_2O_6$, indicating a change in $FeMn(NbTa)_2O_6$ microstructure. From surface topographical analysis, the root-mean-square (RMS) roughness was estimated to be 1.72 nm for $FeNb_2O_6$ and 2.91 nm

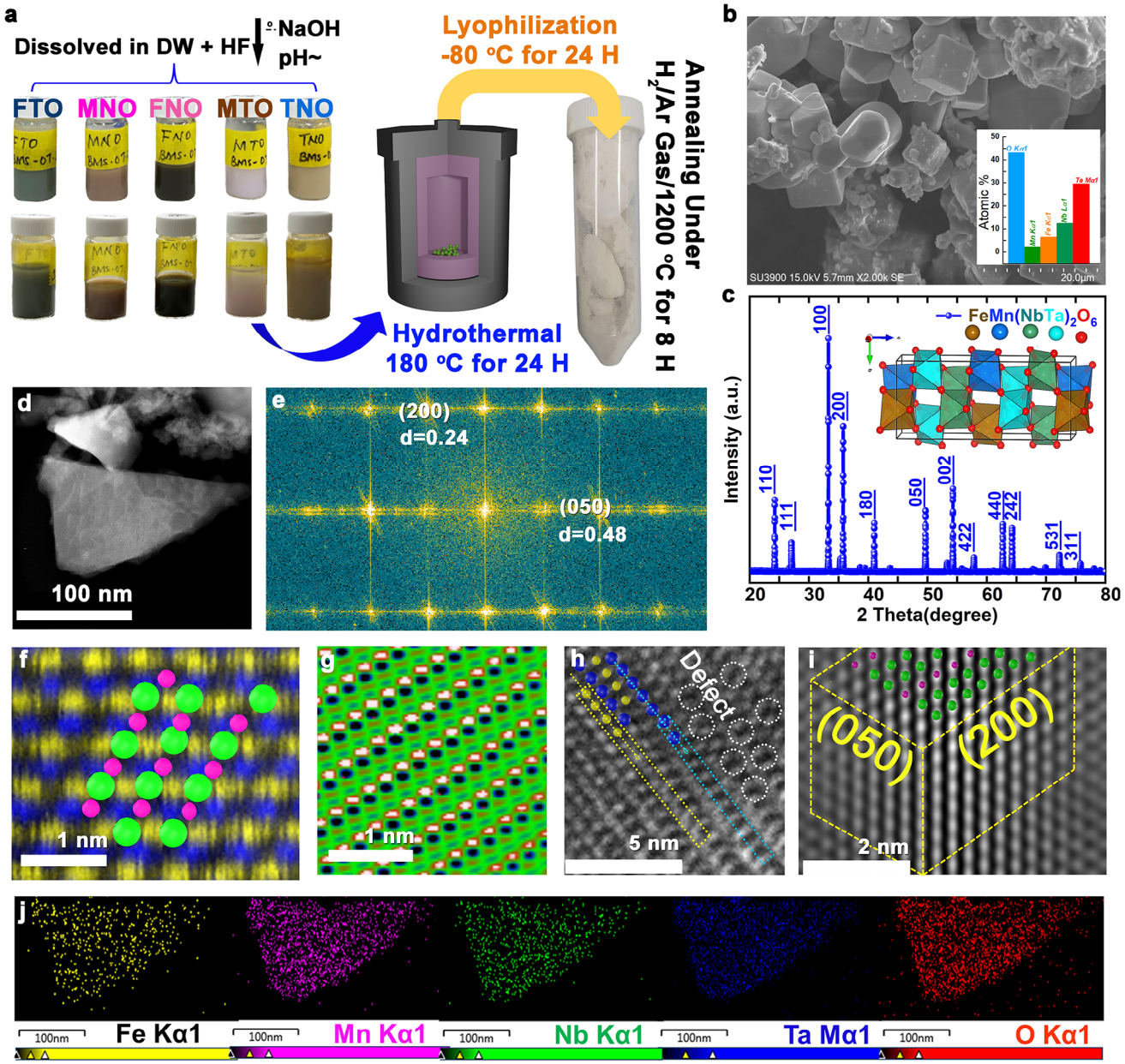

Figure 1. Preparation, Morphological, and Microstructural Characterization of $FeMn(NbTa)_2O_6$ Columbite. a) Schematic representation of the preparation process. b) Scanning electron microscopy (SEM) image. Inset displays a bar graph of atomic percentages for Fe, Mn, Nb, Ta, and O. c) Ex situ High-Resolution Powder Diffraction (HRPD) with the inset showing the DFT structural model and atomic arrangements within $FeMn(NbTa)_2O_6$ columbite. d) Transmission electron microscopy (TEM) image. e) Selected area electron diffraction patterns of (050) and (200) crystallographic planes with corresponding d-spacings. (f–h) High-resolution transmission electron microscopy (HRTEM) images illustrating the atomic arrangement and presence of structural defects in $FeMn(NbTa)_2O_6$. i) Annular Dark Field (ADF) image of $FeMn(NbTa)_2O_6$, aligned along the (050) and (200) crystallographic planes of the octahedral framework. j) Elemental mapping through EDS displaying the distribution of Fe-Kα1, Mn-Kα1, Nb-Kα1, Ta-Mα1, and O-Kα1.

for $FeMn(NbTa)_2O_6$, suggesting $FeMn(NbTa)_2O_6$ has a more porous surface than $FeNb_2O_6$. Additionally, the morphology and composition of $FeNb_2O_6$, $FeTa_2O_6$, $MnNb_2O_6$, $MnTa_2O_6$, and $FeMn(NbTa)_2O_6$ were characterized by scanning electron microscopy (SEM), depicting an irregular shape with slight local nanocrystal aggregation (Figure S2, Supporting Information). Results from energy-dispersive X-ray spectroscopy (EDS) indicated that the final columbite cation ratios were consistent with the initial ratios of their metal precursors (Figure S9, Supporting Information).

High-resolution scanning transmission electron microscopy (HR-STEM) and transmission electron microscopy (TEM) images (Figure 1d, Figure S10, Supporting Information) clearly show that $FeMn(NbTa)_2O_6$ nanoparticles exhibit irregular sizes. In Figure S11, Supporting Information, $FeMn(NbTa)_2O_6$ displays perpendicularly oriented twin planes (red and pink

outlines). We further enlarged the selected rectangular areas from
Figure S12, Supporting Information, plotting rectangular-scanning intensity profiles (matching red/pink colors) with interlayer distances (d) of 0.48 nm and 0.117 nm, corresponding to resolved [050] zone axes. The corresponding fast Fourier transform (FFT) pattern (Figure 1e) identifies the exposed [200] planes with d = 0.48 nm, and the columbite planes along the [050] zone axes with d = 0.24 nm. This suggests that the atoms in $FeMn(NbTa)_2O_6$ are arranged in an octahedral structure (*Pbcn*), specifically connected at the corners with four Fe-MnO_6 octahedra. Here, one edge is shared with an Nb-TaO_6 octahedron, and another edge is shared with an Fe-MnO_6 octahedron. Such characteristics produce a unique crystal structure with corner-sharing octahedral tilt angles ranging from 36°–59°, consistent with selected area electron diffraction (SAED) findings (Table S1, Supporting Information).

A red-green-blue (RGB) high-magnification HAADF–STEM image (Figure 1f, Figures S16–S19, Supporting Information) displays the elemental distribution of $FeMn(NbTa)_2O_6$, with yellow centers corresponding to areas with higher atomic element numbers (B-site cations). In contrast, blue spots correspond to neighboring atoms with lower atomic numbers, such as A-site cations. The embedded inset image of the $FeMn(NbTa)_2O_6$ crystal structure aligns well with the measured RGB-HAADF-STEM data. Figure 1g shows a typical atomic-resolution annular bright field (ABF) image, which confirms the atomic arrangement of the regular octahedral structure. The ABF image also reveals crystalline defects in Figure 1h introduced by high-density atoms, which can create uneven charge distributions and modify the electronic properties of A-site cations in octahedral coordination during annealing at 1200 °C.

The annular dark field (ADF) image in Figure 1i reveals the presence of metallic centers in $FeMn(NbTa)_2O_6$ nanoparticles, well-aligned along the [050] and [200] planes of the octahedral framework, as indicated by the white circled spots. This observation is consistent with the cation stacking sequence AB-BABB in the crystal structure, as shown in Figures S11–S18, Supporting Information. Fe, Mn, Ta, Nb, and O ions (Figure 1j, Figure S20, Supporting Information) are homogeneously distributed, as demonstrated by the overlapped HAADF-EDS, image. This porosity could provide additional active sites for the electrochemical reactions leading to enhanced activity.

The compositions and chemical states of $FeNb_2O_6$, $FeTa_2O_6$, $MnNb_2O_6$, $MnTa_2O_6$, and $FeMn(NbTa)_2O_6$ nanoparticles (NPs) were analyzed by X-ray photoelectron spectroscopy (XPS). The survey spectrum confirms the presence of all chemical elements as shown in Table S2, Supporting Information, including Mn, Fe, Nb, Ta, and O. The Fe 2*p* spectra of $FeTa_2O_6$, $FeNb_2O_6$, and $FeMn(NbTa)_2O_6$ (**Figure 2a**) exhibit two distinct peaks corresponding to Fe $2p_{3/2}$ spin at ≈710 (satellite at ≈718.7 eV) and ≈723 eV (satellite at ≈733.4 eV) in the FeO_6 octahedra at the A-site, indicating the presence of both Fe^{+2} and Fe^{+3} oxidation states. In particular, the Fe^{2+} oxidation state is characterized by peaks at 709.5, 709.2, and 709.6 eV in $FeTa_2O_6$, $FeNb_2O_6$, and $FeMn(NbTa)_2O_6$, respectively. Likewise, the Fe^{3+} oxidation state (Fe_3O_4) is characterized by peaks at 711.2, 712.0, and 712.3 eV in $FeTa_2O_6$, $FeNb_2O_6$, and $FeMn(NbTa)_2O_6$, respectively. These slight variations in binding energy are attributed to differences in the chemical environments of FeO_6 octahedra. The presence of both oxidation states suggests Fe can participate in the final step of O_2 formation, with the +3 oxidation state promoting the formation of OH^-; this can further react to form O_2 during OER.[25] Figure 2b shows Mn 2*p* cores in $MnNb_2O_6$, $MnTa_2O_6$, and $FeMn(NbTa)_2O_6$ nanoparticles have two spin-orbit peak doublets associated with MnO_6 frameworks at the A-sites, with their lowest binding energy at ≈640.6 eV (satellite at 644.5 eV in Mn $2p_{3/2}$) and their highest binding energy at ≈652.3 eV for Mn $2p_{1/2}$. The XPS spectrum of Mn 2*p* in MnO_6-based materials displays distinct peaks corresponding to different Mn oxidation states. In particular, peaks at 639.7, 640.6, and 639.9 eV correspond to the Mn^{2+} oxidation state (MnO species) in $MnTa_2O_6$, $MnNb_2O_6$, and $FeMn(NbTa)_2O_6$, respectively. On the other hand, peaks at 641.4, 642.1, and 641.6 eV correspond to the Mn^{3+} oxidation state in $MnNb_2O_6$, $MnTa_2O_6$, and $FeMn(NbTa)_2O_6$, respectively. Slight variation in the binding energies of Mn in these materials is an indication of differences in the chemical environments of MnO_6 octahedra. The presence of Mn with both Mn^{+2} and Mn^{+3} oxidation states suggests that Mn can act as a redox mediator, facilitating electron transfer during the OER.[9,26] Additionally, slight changes in the binding energy of Mn in different chemical environments indicate the presence of different active sites with varying reactivity toward OER.[27] In Figure 2c, Nb 3*d* spectra of $FeNb_2O_6$ and $MnNb_2O_6$ display two peaks with small shifts in $3d_{5/2}$ (205.9 and 205.8 eV) and $3d_{3/2}$ (208.7 and 208.6 eV), which are similar to those of Nb_2O_5 and are thus attributed to Nb^{5+} ions. In contrast, Nb $3d_{5/2}$ and $3d_{3/2}$ peaks of $FeMn(NbTa)_2O_6$ were positively shifted to 206.2 and 208.9 eV, respectively. As shown in Figure 2d, the spectrum was deconvoluted into two spin-orbit peaks – with the lowest binding energy at ≈25.0 eV (Ta $4f_{7/2}$) and the highest binding energy at ≈26.8 eV (Ta $4f_{5/2}$) – for $FeTa_2O_6$, $MnTa_2O_6$, and $FeMn(NbTa)_2O_6$ coordinated in TaO_6 octahedra at B-sites. Moreover, Ta 4*f* of $FeMn(NbTa)_2O_6$ also features slightly more positive binding energies compared to those of $MnTa_2O_6$ or $FeTa_2O_6$. The observed positive shift indicates how Fe or Mn at A-sites modify charge distributions in $FeMn(NbTa)_2O_6$ lattices. This, in turn, has a significant impact on the oxidation states of Fe and Mn at A-sites. Such changes ultimately influence the electronic properties of $FeMn(NbTa)_2O_6$, including its ability to facilitate electron transfer between H_2O and Fe/Mn active sites.[28] The mixed high valence states of Nb and Ta at BO_6-sites could also contribute to stabilizing intermediate species generated during the OER, thus enhancing $FeMn(NbTa)_2O_6$ catalytic activity.[29] Meanwhile, O 1*s* spectra in Figure 2e exhibit three peaks that correspond to O-metal (≈528.8 eV), O-defect (≈530.3 eV), and O-carbon (532.6 eV) bonding in $FeNb_2O_6$, $FeTa_2O_6$, $MnNb_2O_6$, $MnTa_2O_6$, and $FeMn(NbTa)_2O_6$. Compared with O 1*s* in $FeMn(NbTa)_2O_6$, other spectra were slightly positively shifted. The ratio between the areas of O-metal and O-defect bonding in $FeMn(NbTa)_2O_6$ significantly changed, showing the chemical environments around oxygen atoms in $FeMn(NbTa)_2O_6$ are different from those around oxygen atoms in $FeNb_2O_6$, $FeTa_2O_6$, $MnNb_2O_6$, and $MnTa_2O_6$. This difference in chemical environments could affect electron densities around oxygen atoms, and thus cause shifting in O 1*s* peaks. Moreover, core-level binding energy peaks (Figure 2f) revealed mappings of valence states in $FeNb_2O_6$, $MnNb_2O_6$, and $FeMn(NbTa)_2O_6$. The peak between 0 and 6 eV could correspond to 2*p* oxygen (O 2*p*) core-level

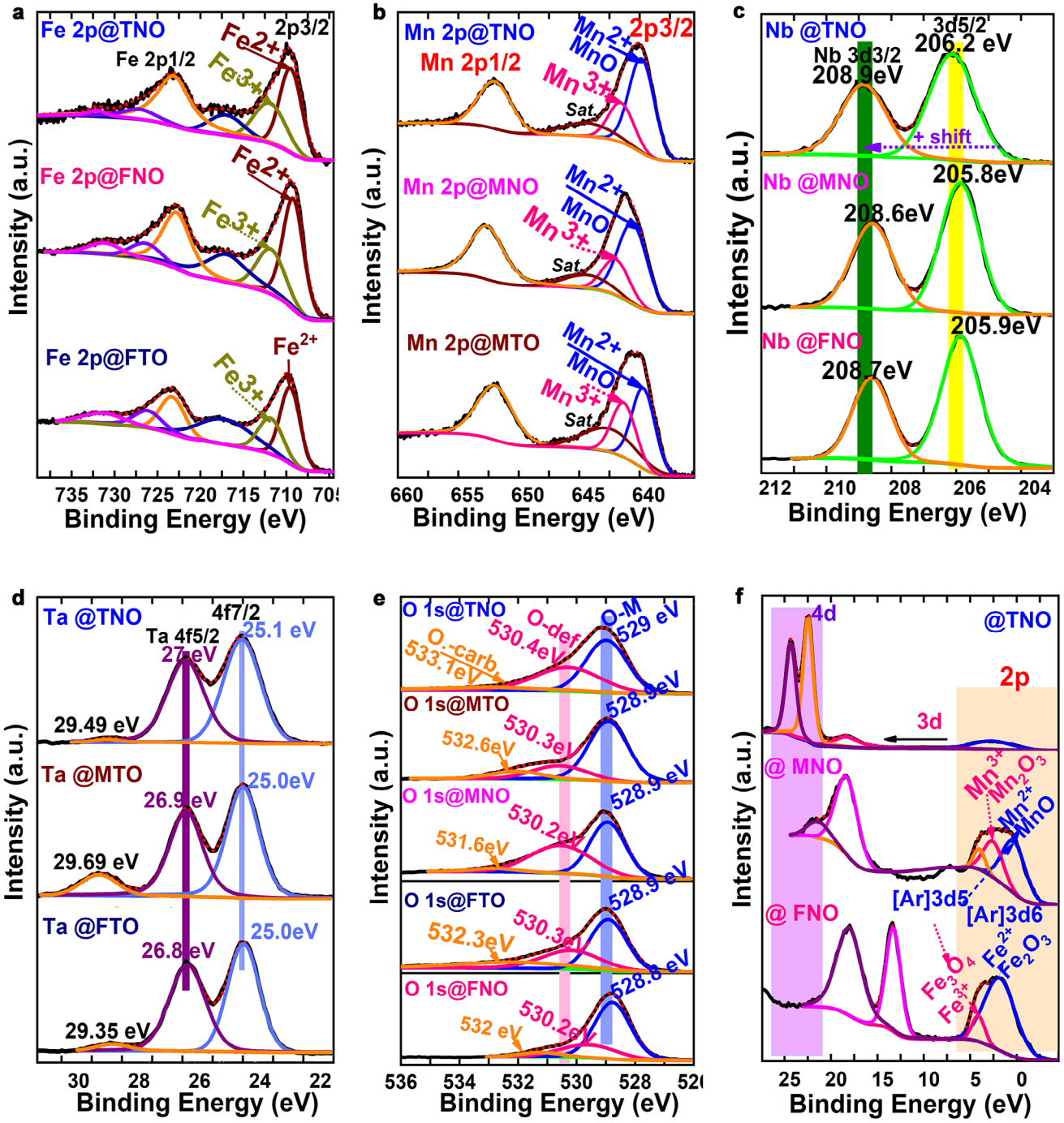

Figure 2. Chemical states characterization. a) Fe 2*p* spectra in $FeNb_2O_6$ (FNO), $FeTa_2O_6$ (FTO), and $FeMn(NbTa)_2O_6$ (TNO). b) Mn 2*p* core level spectra of $MnNb_2O_6$ (MNO), $MnTa_2O_6$ (MTO), and $FeMn(NbTa)_2O_6$. c) Nb 3*d* spectra of $FeNb_2O_6$, $MnNb_2O_6$, and $FeMn(NbTa)_2O_6$. d) Ta 4*f* spectra of $FeTa_2O_6$, $MnTa_2O_6$, and $FeMn(NbTa)_2O_6$. e) O 1*s* spectra of $FeNb_2O_6$, $FeTa_2O_6$, $MnNb_2O_6$, $MnTa_2O_6$, and $FeMn(NbTa)_2O_6$. f) Valence states mapped to corresponding spectral peaks in $FeNb_2O_6$, $MnNb_2O_6$, and $FeMn(NbTa)_2O_6$.

electrons, such as those from $Fe^{2+}[Ar]3d^6$, $Fe^{3+}[Ar]3d^5$ in Fe_2O_3 or $Mn^{2+}[Ar]3d^5$, and Mn^{3+} in Mn_2O_3. The binding energy range of 7–12 eV is consistent with the 3*d* core-level electrons of Mn, while the two closely spaced peaks between 12 and 27 eV are consistent with the 4*d* core-level electrons of Nb and Ta with +5 valence states.

The local coordination environments of Fe, Mn, Nb, and Ta elements were further investigatedby X-ray absorption spectroscopy (XAS), confirming formal oxidation states of Mn^{2+}, Fe^{2+}, Nb^{5+}, and Ta^{5+} cations within $FeNb_2O_6$, $FeTa_2O_6$, $MnNb_2O_6$, $MnTa_2O_6$, and $FeMn(NbTa)_2O_6$-columbite when paired with XPS analyses. In Figure S21a, Supporting Information, X-ray absorption

near-edge structure (XANES) spectra show both $FeNb_2O_6$ and $FeMn(NbTa)_2O_6$ have high Fe oxidation states compared to Fe coltan rock salt. In these ex situ Fe *K*-edge XANES spectra, the pre-edge peak ≈7114 eV originates from a 1*s*→3*d* transition. Meanwhile, the corresponding white line originates from a 1*s*→4*p* transition. White lines of the Fe *K*-edge demonstrate that $FeMn(NbTa)_2O_6$ has more occupied electronic states than FNO, as supported by EXAFS results. Further, ex situ Mn *K*-edges of $FeMn(NbTa)_2O_6$ (Figure S22, Supporting Information) exhibit higher oxidation states than MTO and MNO, which featured lower Mn valence states than 3+ or 4+ references. The pre-edge peak at 6539 eV verified that $MnNb_2O_6$, $MnTa_2O_6$, and $FeMn(NbTa)_2O_6$ are octahedral structures, with $FeMn(NbTa)_2O_6$ having more *d*-site electron occupancy due to its larger pre-edge peak. In Figure S21b, Supporting Information, the absorption Nb *K*-edge peak positions of FNO and $FeMn(NbTa)_2O_6$ are consistent with Nb^{5+}, as compared with Nb_2O_5 or rock coltan. The white line of the Ta *L*-edge (Figure S21c, Supporting Information) is higher than that of rock coltan, which means that $FeMn(NbTa)_2O_6$ features more *p*→*d* based transition states than other columbites.

The Fourier-transformed EXAFS offers a detailed view of the local environments of the metal-oxygen bonds localized ≈1.52 Å, with longer metallic-metallic pathways of up to 2.74 Å between A and B sites when atomic phase shifts were not considered. The comparison of $FeMn(NbTa)_2O_6$ with $MnNb_2O_6$ and $MnTa_2O_6$ in Figures S23–S26 and Tables S3–S5, Supporting Information reveals notable differences in the local coordination environments of their Mn cations. In $MnNb_2O_6$, Mn is coordinated with O (Mn-O1: CN = 1.5, bond length = 1.90 Å, σ^2 = 0.008 Å^2; Mn-O2: CN = 4.0, bond length = 2.21 Å, σ^2 = 0.011 Å^2), Nb (Mn-Nb: CN = 3.5, bond length = 3.07 Å, σ^2 = 0.012 Å^2), and other Mn (Mn-Mn: CN = 6.0, bond length = 3.14 Å, σ^2 = 0.008 Å^2). In $MnTa_2O_6$, Mn shows a higher coordination with O (Mn-O1: CN = 4.5, bond length = 1.94 Å, σ^2 = 0.010 Å^2), and a more prominent coordination with Ta (Mn-Ta: CN = 8.0, bond length = 3.17 Å, σ^2 = 0.005 Å^2). When compared to $FeMn(NbTa)_2O_6$ – which exhibits coordination with Nb (Mn-Nb: CN = 2.5, bond length = 2.74 Å, σ^2 = 0.005 Å^2), Ta (Mn-Ta: CN = 3.0, bond length = 3.35 Å, σ^2 = 0.006 Å^2), and O (Mn-O1: CN = 3.5, bond length = 2.03 Å, σ^2 = 0.004 Å^2) – the presence of Fe significantly influences Mn coordination environments, particularly bond lengths and Debye-Waller factors. The wavelet transforms (WT) in Figure S26, Supporting Information depict O within lower *k*-space magnitudes, and metal distributions within higher *k*-space magnitudes. Note that the WT contour plot of Mn foils had only one intensity maximum of ≈5.5 Å^{-1} in *k*-space, corresponding to metallic Mn-Mn coordination. As for $MnTa_2O_6$, three obvious intensity maxima at 3.5, 4.5, and 8.5 Å^{-1} were observed from WT contour plots, which were respectively attributed to Mn-O1, Mn-O2, and Mn-Ta scattering paths. $MnNb_2O_6$ exposed two intensity maxima at 3.5 and 6.5 Å^{-1}, corresponding to Mn-O and Mn-Nb. In $FeMn(NbTa)_2O_6$ samples, Mn-O was localized at 4.5 Å^{-1} in *k*-space, while Mn/Fe/Nb/Ta pathways were found ≈6 Å^{-1} in *k*-space.

The pre-edge XANES peak locations and coordination environments of cationic sites in the $FeMn(TaNb)_2O_6$ system align with both ex situ high-resolution powder diffraction (HRPD) patterns and the DFT model. These findings confirm the alternating positions of Fe and Mn at the A-sites, and Nb and Ta at the B-sites, consistent with the RGB high-magnification HAADF–STEM image of $FeMn(TaNb)_2O_6$ in Figure 1f. This consistency between the ex situ XANES, HRPD, and HAADF–STEM results reinforces the structural model and enhances confidence in the cation site occupancies.

2.2. Catalytic Performance Evaluation of OER and HER

The redox activities of $FeMn(NbTa)_2O_6$ and related columbite electrocatalysts were determined through cyclic voltammetry (CV) and linear sweep voltammetry (LSV) measurements. We initially investigated the electrochemical redox activities of $FeMn(NbTa)_2O_6$, $FeNb_2O_6$, $FeTa_2O_6$, $MnNb_2O_6$, and $MnTa_2O_6$ for the oxygen evolution reaction (OER) by conducting an extended CV analysis, namely under an electrochemical domain of 1.1–2.0 V vs. RHE. Given that $FeMn(NbTa)_2O_6$, $FeNb_2O_6$, and $FeTa_2O_6$ (Figure S27, Supporting Information) have Fe^{2+} in their structures, they exhibit Fe^{2+}/Fe^{3+} oxidation peaks evaluated at 1.48, 1.46, and 1.43 V vs. RHE, respectively. In contrast, $MnNb_2O_6$ and $MnTa_2O_6$ catalysts (Figure S27, Supporting Information), containing Mn^{2+} display Mn^{2+}/Mn^{3+} oxidation peaks at 1.38 and 1.40 V vs. RHE, preceding the onset of OER. Interestingly, $FeMn(NbTa)_2O_6$ reaches an oxidation peak at 1.56 V vs. RHE at a current density of 100 mA/cm^2 without iR correction, whereas $FeNb_2O_6$, $FeTa_2O_6$, $MnNb_2O_6$, and $MnTa_2O_6$ require slightly higher potentials of 1.65, 1.69, 1.63, and 1.67 V vs. RHE, respectively, at the same current density. These results suggest that redox reactions involving 3*d*, 4*d*, and 5*d* in catalysts crucially impact the oxygen evolution process. However, the observed differences in potential requirements for OER initiation provide insights into associated catalytic activities and energy barriers. $FeMn(NbTa)_2O_6$ catalysts stand out with their lower potential requirements, indicating possibly enhanced catalytic efficiency or more favorable redox properties for OER initiation.

As shown in the linear sweep voltammetry (LSV) curves (**Figure 3a**), $FeMn(NbTa)_2O_6$-1200, $MnNb_2O_6$, and $FeMn(NbTa)_2O_6$-110 achieved respective voltages of 1.53, 1.58, and 1.59 V vs. RHE at the current density of 50 mA cm^{-2}. These values surpass the performance of RuO_2 (j = 1.61 V vs. RHE at 50 mA cm^{-2}), nickel foam (j = 1.76 V vs. RHE), and $MnTa_2O_6/FeTa_2O_6$ (j = 1.60 V vs. RHE) at the same current density. Among these, $FeMn(NbTa)_2O_6$-1200 demonstrated the best OER performance with an overpotential of 300 mV at 50 mA cm^{-2}, one of the lowest overpotentials reported among OER catalysts. Under high current density (j_{2nn} = 200 mA cm^{-2}), the OER activity of AB_2O_6 catalysts with a 16.8 mg mass loading was compared to state-of-the-art RuO_2/C. As shown in Figure 3b, Fe-Mn-O based $FeMn(NbTa)_2O_6$ maintained stable OER activity with an overpotential of 419 mV at 200 mA cm^{-2} until the end of the reaction. This performance surpasses that of $MnNb_2O_6$ (508 mV), $FeNb_2O_6$ (537 mV), $MnTa_2O_6$ (571 mV), and $FeTa_2O_6$ (613 mV), as well as the RuO_2 benchmark (652 mV) and nickel foam (1012 mV). The coexistence of Fe and Mn cations, likely through coordination with oxygen in FeO_6 and MnO_6 octahedra, plays a crucial role in enhancing the OER activity.

To gain a deeper understanding of OER kinetics, Tafel slopes were obtained by analysing the LSV polarization

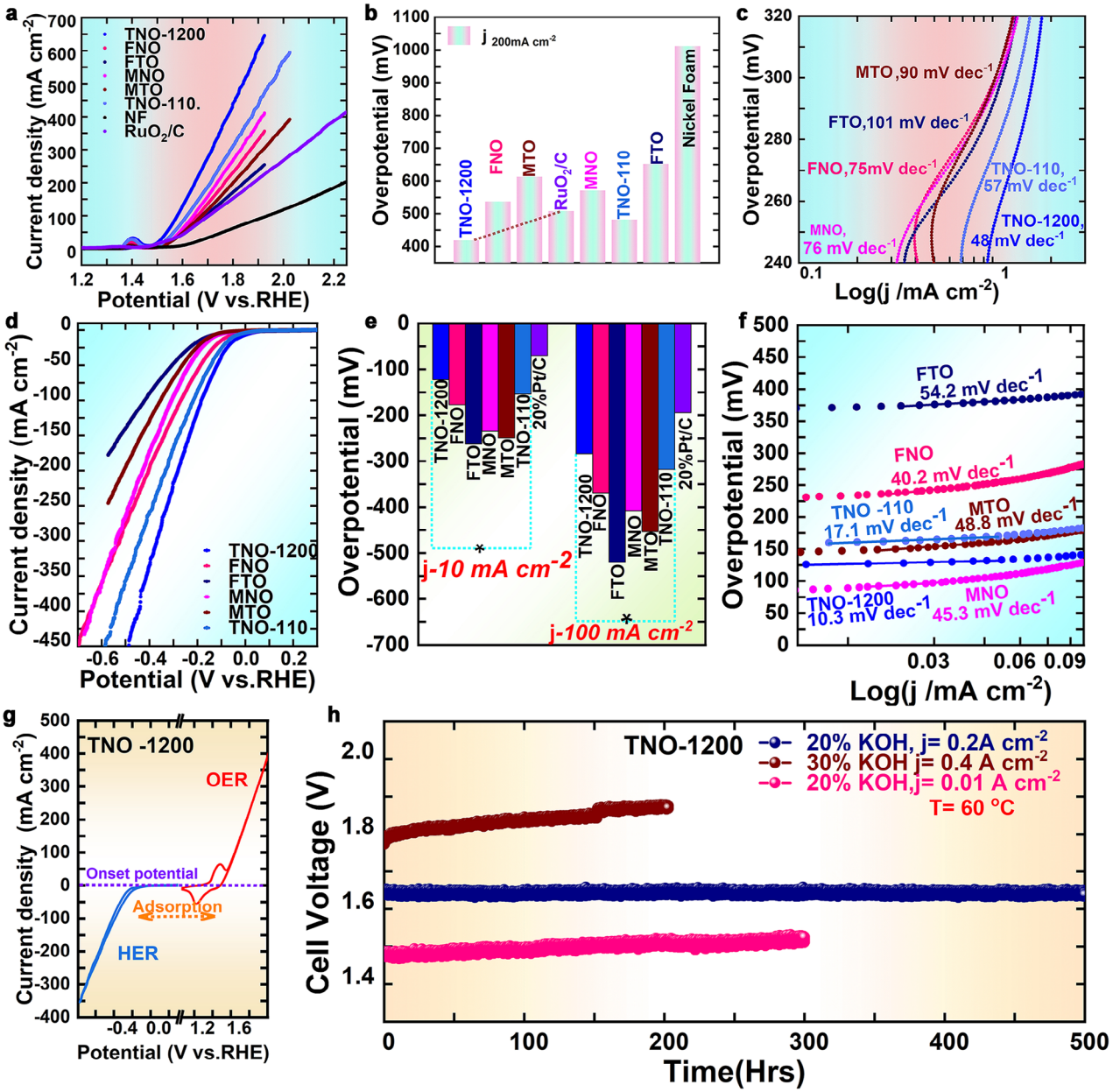

Figure 3. Electrochemical Performance of $FeMn(NbTa)_2O_6$ Catalysts for OER and HER. a) Oxygen evolution reaction (OER) polarization curves for $FeMn(NbTa)_2O_6$-1200 (TNO-1200), $FeNb_2O_6$ (FNO), $FeTa_2O_6$ (FTO), $MnNb_2O_6$ (MNO), $MnTa_2O_6$ (MTO), and $FeMn(NbTa)_2O_6$-110 (TNO-110), compared to nickel foam (NF) and RuO_2/C benchmarks. b) Overpotential at j = 200 mA cm^{-2} for $FeMn(NbTa)_2O_6$-1200 (TNO-1200), $FeNb_2O_6$ (FNO), $FeTa_2O_6$ (FTO), $MnNb_2O_6$ (MNO), $MnTa_2O_6$ (MTO), and $FeMn(NbTa)_2O_6$-110 (TNO-110), compared to NF and RuO_2/C. c) Tafel slopes of the same electrocatalysts, highlighting OER kinetics. d) Hydrogen evolution reaction (HER) polarization curves for $FeMn(NbTa)_2O_6$-1200 (TNO-1200), $FeNb_2O_6$ (FNO), $FeTa_2O_6$ (FTO), $MnNb_2O_6$ (MNO), $MnTa_2O_6$(MTO), and $FeMn(NbTa)_2O_6$-110 (TNO-110), measured in N_2-saturated 1 M KOH at a scan rate of 2 mV s^{-1}. e) HER activity of $FeMn(NbTa)_2O_6$-1200, $FeNb_2O_6$, $FeTa_2O_6$, $MnNb_2O_6$, $MnTa_2O_6$, and $FeMn(NbTa)_2O_6$-110 at current densities of j = 10 and 100 mA cm^{-2}. f) HER Tafel plots for the same electrocatalysts, highlighting HER kinetics. g) Combined OER and HER polarization curves of $FeMn(NbTa)_2O_6$(TNO-1200). h) Stability plot for $FeMn(NbTa)_2O_6$-1200 spray-coated on nickel foam electrodes at current densities of 0.01, 0.2, and 0.4 A cm^{-2}, measured at 60 °C in 20% and 30% KOH solutions.

curves (Figure 3c). Among the AB_2O_6-columbite catalysts, $FeMn(NbTa)_2O_6$-1200 and $FeMn(NbTa)_2O_6$-110 exhibited the smallest Tafel slopes of 48 and 57 mV dec^{-1}, indicating the fastest reaction rates. These values are significantly lower compared to the other catalysts, such as $FeNb_2O_6$ (≈78 mV dec^{-1}), $MnNb_2O_6$ (75 mV dec^{-1}), $MnTa_2O_6$ (90 mV dec^{-1}), and $FeTa_2O_6$ (168 mV dec^{-1}). These results indicate that the number of electrons transferred during the rate-determining transition states differ across the $FeMn(NbTa)_2O_6$, $FeNb_2O_6$, $MnNb_2O_6$, $MnTa_2O_6$, and $FeTa_2O_6$ catalysts, differentially promoting the

OER at low overpotentials.[30] Moreover, the electrochemical surface area (ECSA), which is associated with double-layer capacitance (C_{dl}), was determined (Figures S28 and S29a, Supporting Information) for $FeMn(NbTa)_2O_6$-1200 (2.08 mF cm^{-2}), $FeMn(NbTa)_2O_6$-110 (1.39 mF cm^{-2}), $FeNb_2O_6$ (0.89 mF cm^{-2}), $MnNb_2O_6$ (1.71 mF cm^{-2}), $MnTa_2O_6$ (1.62 mF cm^{-2}), and $FeTa_2O_6$ (0.90 mF cm^{-2}). These were determined from the no-Faradaic zone on the CV function of potential (0.1–0.2 V vs. RHE) over different scan rates, reflecting electrical charge that accumulates at electrode surfaces. The results showed that $FeMn(NbTa)_2O_6$-1200 had the highest C_{dl} value of 2.08 mF cm^{-2}, indicating a large electrochemical surface area. This suggests that $FeMn(NbTa)_2O_6$-1200 has a higher density of active sites available for catalysis than other metal oxides, thus MnO_6 and FeO_6 sites are possibly critical to the adsorption and activation of reactants.[31] $FeMn(NbTa)_2O_6$ mass activity (mass loaded: 16.8 mg, mass molar: 214.33 g mol^{-1}) at $j_{50mA/cm2}$ = 300 mV was estimated with the following equation: mass activity = current at $j_{50mA/cm2}$ / moles $FeMn(NbTa)_2O_6$.

The estimated mass activity of the $FeMn(NbTa)_2O_6$ electrode was 3.2×10^8 mA g^{-1}. The turnover frequency (TOF in Supporting Information) is determined to be 2.58×10^{-4} s^{-1}, confirming its high intrinsic electrocatalytic performance, as it shows the rate at which the OER reaction occurs per active site on the $FeMn(NbTa)_2O_6$ electrode. Nyquist cycles from electrochemical impedance spectroscopy (EIS) measurements was used to evaluate charge transfer resistance (R_{ct}) under AC impedance. As demonstrated in Figure S29b, Supporting Information, the Nyquist plot of $MnNb_2O_6$ shows a smaller quasi-semicircle than other materials such as $FeMn(NbTa)_2O_6$, namely due to its lower charge transfer resistance. Through accelerated electron transfer kinetics in the reaction $2H_2O + 4O^* \rightarrow 4OH^* + O_2 + 4e^-$, $FeMn(NbTa)_2O_6$ and other materials are oxidized and lose electrons, while water is reduced to produce oxygen and protons. The Bode plots of $FeMn(NbTa)_2O_6$, $FeNb_2O_6$, $FeTa_2O_6$, $MnNb_2O_6$, and $MnTa_2O_6$ conducted at 1.53 V vs. RHE (Figure S29c, Supporting Information) indicate that observed frequency-dependent reaction mechanisms produce unique electrochemical reaction processes on catalytic surfaces. The Bode plots of $FeMn(NbTa)_2O_6$-1200, $FeMn(NbTa)_2O_6$-110, $FeNb_2O_6$, $FeTa_2O_6$, $MnNb_2O_6$, and $MnTa_2O_6$ catalysts were evaluated and compared at the open circuit potential (OCP), 1.48, 1.54, and 1.67 V vs. RHE to observe responses to OER activity. In the high-frequency region (4–5 Hz), $MnNb_2O_6$ and $FeTa_2O_6$ peaks overlap, indicating strong adsorption interactions of OH^- with AO_6 (A = Fe, Mn). The strength of M-OH interactions is influenced by metal center coordination environments of FeO_6 and MnO_6 polyhedra, affecting the orientation of OH^- on surfaces and how strongly OH^- interacts with neighboring metals (Ta, Nb) on $FeMn(NbTa)_2O_6$ catalysts.[32] Therefore, Nb ($4d^45s^1$, with 5 valence electrons in 4*d* and 5*s* orbitals) and Ta ($4f^{14}5d^36s^2$, with 5 valence electrons in 5*d* and 6*s* orbitals) in $FeMn(NbTa)_2O_6$ have high *d*-band centers and exhibit stronger interactions with OH^- due to decreased filling of their anti-bonding states. While double-layer capacitance in the low-frequency range is controlled by diffusion processes, peaks in this region also change as different potentials are applied and as composition is varied. Such peak shifts at high phase angles indicate the diffusion process changes, controlling double-layer capacitance in this range.

For example, FeO_6 will oxidize via $FeO_6 + 3OH^- + H_2O \rightarrow FeOOH + 3O_2 + 2H_2O$ and MnO_6 through $MnO_6 + OH^- + H_2O \rightarrow MnO_4^- + 2H_2O + e^-$ in $FeMn(NbTa)_2O_6$. At the OCP, wherein the working electrode is in an electrochemical equilibrium state, $FeMn(NbTa)_2O_6$-1200 exhibited high-frequency relaxation during double-layer capacitance. This demonstrates strong adsorption of oxygen species. As we set up the potential at 1.48 V vs. RHE, $FeMn(NbTa)_2O_6$ frequency started to decrease during double layer capacitance upon domination by adsorption of oxygen species. At increased potentials such as 1.54 V vs. RHE, the double-layer capacitance became more significant due to the oxidation of Fe and Mn centers, forming FeOOH and $MnO_x(OH)_y$. At 1.67 V vs. RHE, the reaction pathway leading to the formation of O_2 involves the transfer of multiple electrons, which results in a change of the charge density and structure of the electrode surface. This is illustrated through the equation below:

$MnO_2 + 4H^+ + 2e \leftrightharpoons Mn^{2+} + 2H_2O$	$E^0 = 1.22$ V
$Ta_2O_5 + Nb_2O_5 + MnO_2 + 2Fe_2O_3 + 32OH^- + 26e \leftrightharpoons 2Ta + 4FeOH^+ + Mn^{2+} + 2Nb + 14H_2O$,	$E^0 = 1.48$ V
$4FeMn(NbTa)_2O_6 + 14H_2O \rightarrow 4FeO(OH) + 4MnO(OH) + 2NbO(OH) + 2TaO(OH) + 4O_2 + 8OH^- + 8e^-$.	$E^0 = 1.48$ V

It had been observed that in the equation,

$$4FeMn(NbTa)_2O_6 + 14H_2O \rightarrow 4FeO(OH) + 4MnO(OH) + 2NbO(OH) + 2TaO(OH) + 4O_2 + 8OH^- + 8e^- \quad (1)$$

adsorbed -OH and -O intermediates are both involved on both sides of the rate-determining step at E^0 = 1.48 V.[33] Similarly, within the potential range of 0.17 to 0.48 V, the corresponding cyclic voltammetry plots (Figure S30, Supporting Information), reveal the distinct involvement of oxygen species. These segments demonstrate cumulative charge transfers ranging from $-8.3x10^3$ to $4.4x10^2$C, indicating diverse electrochemical processes associated with the redox reactions of oxygen species over this voltage window. The adsorption of oxygen species and observed redox reactions throughout the cycles (Figure S31, Supporting Information) reveal dynamic processes at the electrode-electrolyte interface. Significant variations in transferred charges indicate pronounced adsorption-redox activity. The formation of OH on Fe and Mn could occur, strongly depending on the level of *d*-electron occupancy of anti-bonding orbitals.[34] Previous studies based on perovskites have shown that Fe and Mn elements in a 3*d* configuration follow common mechanisms for oxygen evolution reactions.[35] This mechanism typically involves the adsorption of OH^- ions followed by rate-determining electrochemical desorption, leading to the formation of peroxyl radicals (OOH). Subsequently, peroxyl radicals undergo catalytic decomposition, thereby producing O_2.[36]

The same behavior over time has been observed (Figure S32a, Supporting Information) with the gradual elevation of potential, caused by gas bubble formation hindering full electrolyte contact with coating materials, leading to decreased reaction rates

and electrode degradation. Lastly, $FeMn(NbTa)_2O_6$ coating surfaces tend to be vulnerable to contamination from by-products and hydride formation during electrochemical reactions, which occur in high-concentration KOH electrolytes at elevated temperatures while applying constant current over time. The accumulation of contaminants on electrode surfaces functions to produce nucleation sites for forming hydrides at elevated temperatures. Therefore, $FeMn(NbTa)_2O_6$ coating surfaces exhibit resilience against challenges affecting current versus temperature relationships. Despite the possibility of contamination from by-products and hydride formation during electrochemical reactions in high-concentration KOH electrolytes at elevated temperatures (Figure 3b), particularly under continuous current application, $FeMn(NbTa)_2O_6$ demonstrates remarkable stability. Even in the face of these conditions, $FeMn(NbTa)_2O_6$ maintains its structural integrity and catalytic activity. The potential accumulation of contaminants on electrode surfaces is effectively mitigated, and $FeMn(NbTa)_2O_6$ continues to perform reliably, showcasing its robustness in various electrochemical environments. Figure S32b, Supporting Information shows that at high current densities, the $FeMn(NbTa)_2O_6$-1200 anode exhibits even better activity than the RuO_2/C commercial catalyst, suggesting an anticipated cost reduction. The superior activity, good stability, and other $FeMn(NbTa)_2O_6$-1200 characteristics improve its economic viability versus conventional RuO_2/C for use in alkaline water electrolyzers. This underscores the potential for the advancement of $FeMn(NbTa)_2O_6$-based materials for large-scale deployment in cost-effective and sustainable energy technologies.

For hydrogen evolution reaction (HER) activity, as shown in Figure 3d, $FeNb_2O_6$, $FeTa_2O_6$, $MnNb_2O_6$, $MnTa_2O_6$, and $FeMn(NbTa)_2O_6$-110 exhibited onset potentials (E_{onset}) of 0.124, 0.225, 0.368, 0.081, 0.141, and 0.157 V vs. RHE at 0.0021 mA cm^{-2}, respectively. At a current of 10 mA cm^{-2}, several of these HER potentials displayed significantly modified onset potential magnitudes without correction. Namely, $FeMn(NbTa)_2O_6$-1200 (−0.125 V vs. RHE), $FeMn(NbTa)_2O_6$-110 (−0.154 V vs. RHE), and $FeNb_2O_6$ (−0.177 V vs. RHE) potentials were relatively unchanged versus those of $MnNb_2O_6$ (−0.235 V vs. RHE), $MnTa_2O_6$ (−0.249 V vs. RHE), and $FeTa_2O_6$ (−0.263 V vs. RHE). This indicates the contributions of Fe and Mn at columbite-tantalite phase A-sites. Interestingly, $FeNb_2O_6$ showed strongly enhanced activity (−0.177 V vs. RHE) versus $MnNb_2O_6$, indicating how interactions between iron and oxygen atoms in FeO_6 octahedra can promote Fe-O-H bond formation; these are essential for the HER, given $MnNb_2O_6$ contains MnO_6 and NbO_6 octahedra as active sites. Notwithstanding its catalytic potential, the Mn-site in $MnNb_2O_6$ exhibits lower activity compared to Fe-sites in $FeNb_2O_6$. This could be attributed to differences in the electronic and structural properties between MnO_6 and FeO_6 octahedra, which influence their ability to facilitate HER. However, $MnTa_2O_6$ and $FeTa_2O_6$ showed reduced HER performance due to interactions between TaO_6 and neighboring octahedra. Furthermore, the Pt/C catalyst exhibits the highest activity, as evidenced by its minimal overpotentials of −70 and −195 mV required to achieve current densities of 10 and 100 mA cm^{-2}, respectively. Similarly, the $FeMn(NbTa)_2O_6$-1200 electrocatalyst demonstrates superior HER activity compared to $FeMn(NbTa)_2O_6$-110, $FeNb_2O_6$, $MnNb_2O_6$, $MnTa_2O_6$, and $FeTa_2O_6$ electrocatalysts in Figure 3e. Interestingly, the $FeMn(NbTa)_2O_6$-1200 catalyst displays smaller overpotentials of −123 and −284 mV to reach current densities of 10 and 100 mA cm^{-2}, respectively. This contrasts with corresponding values for $FeMn(NbTa)_2O_6$-110 (−154 mV, −318 mV), $FeNb_2O_6$ (−177 mV, −369 mV), $MnNb_2O_6$ (−235 mV, −408 mV), $MnTa_2O_6$ (−249 mV, −454 mV), and $FeTa_2O_6$ (−263 mV, −520 mV), indicating enhanced capability in driving the HER with lower energy requirements.

The catalytic kinetics were investigated through HER Tafel plot polarization, as shown in Figure 3f. $FeMn(NbTa)_2O_6$-1200 and $FeMn(NbTa)_2O_6$-110 exhibited respective HER Tafel slopes of 10 and 17 mV dec^{-1}, which were lower than those of $FeNb_2O_6$ (40 mV dec^{-1}), $MnNb_2O_6$ (45 mV dec^{-1}), $MnTa_2O_6$ (49 mV dec^{-1}), and $FeTa_2O_6$ (54 mV dec^{-1}). In an alkaline environment, the HER proceeds through several steps:

- Volmer Step: This initial step involves the dissociation of water molecules and the formation of reactive hydrogen intermediates (H_{ad}), according to the reaction: $H_2O + e^- + M \rightarrow M - H_{ad} + OH^-$. In this step, an electron is transferred to an active site on the catalytic material, resulting in the formation of reactive hydrogen intermediates.
- Tafel Step: After the formation of reactive hydrogen intermediates, the Tafel step occurs. In this step, two reactive hydrogen intermediates ($2M - H_{ad}$) react to form hydrogen molecules (H_2) and regenerate the active site: $2M - H_{ad} \rightarrow H_2 + 2M$.[37]
- Heyrovsky Step: Alternatively, HER can also occur through the Heyrovsky step, where the hydrogen intermediate ($M - H_{ad}$) reacts with a water molecule (H_2O) and an electron to form hydrogen molecules (H_2) and hydroxide ions (OH^-). This regenerates the active site: $H_2O + e^- + M - ad \rightarrow H_2 + OH^- + M$.[38]

Therefore, the presence of FeO_6 and MnO_6 in the $FeMn(NbTa)_2O_6$ structure contributes to a high catalytic activity for HER. The synergistic interactions between Fe ions, Mn ions, and the surrounding ligands facilitate water reduction and the formation of reactive hydrogen intermediates (H_{ad}). This leads to a lower Tafel slope for $FeMn(NbTa)_2O_6$-1200 (10.3 mV dec^{-1}) and $FeMn(NbTa)_2O_6$-110 (17.1 mV dec^{-1}) compared to other mentioned compounds, suggesting the Volmer–Heyrovsky reaction is the dominant HER pathway. In $FeNb_2O_6$, $MnNb_2O_6$, $FeTa_2O_6$, and $MnTa_2O_6$ the presence of A-site atoms in a B-site matrix can influence HER reaction kinetics, resulting in a higher Tafel slope.

To demonstrate comparative improvement in catalytic activity among $FeMn(NbTa)_2O_6$, $FeNb_2O_6$, $MnNb_2O_6$, $FeTa_2O_6$, and $MnTa_2O_6$, electrochemical impedance spectroscopy (EIS) was utilized at different HER overpotentials within this system. The Nyquist and Bode plots depicting EIS responses are presented in Figure S35a, Supporting Information. $FeMn(NbTa)_2O_6$, $FeNb_2O_6$, $MnNb_2O_6$, $FeTa_2O_6$, and $MnTa_2O_6$ electrodes exhibited two semicircles, including the high-frequency and low-frequency regions of all applied potentials; this indicates such electrodes operate under Randles equivalent circuit models. Bode plots (Figure S35b, Supporting Information) obtained from EIS illustrate charge transfer resistance zones in relationship with phase angle (θ). High-frequency regions show resistance to electrolyte solutions, whereas low-frequency regions correspond to working

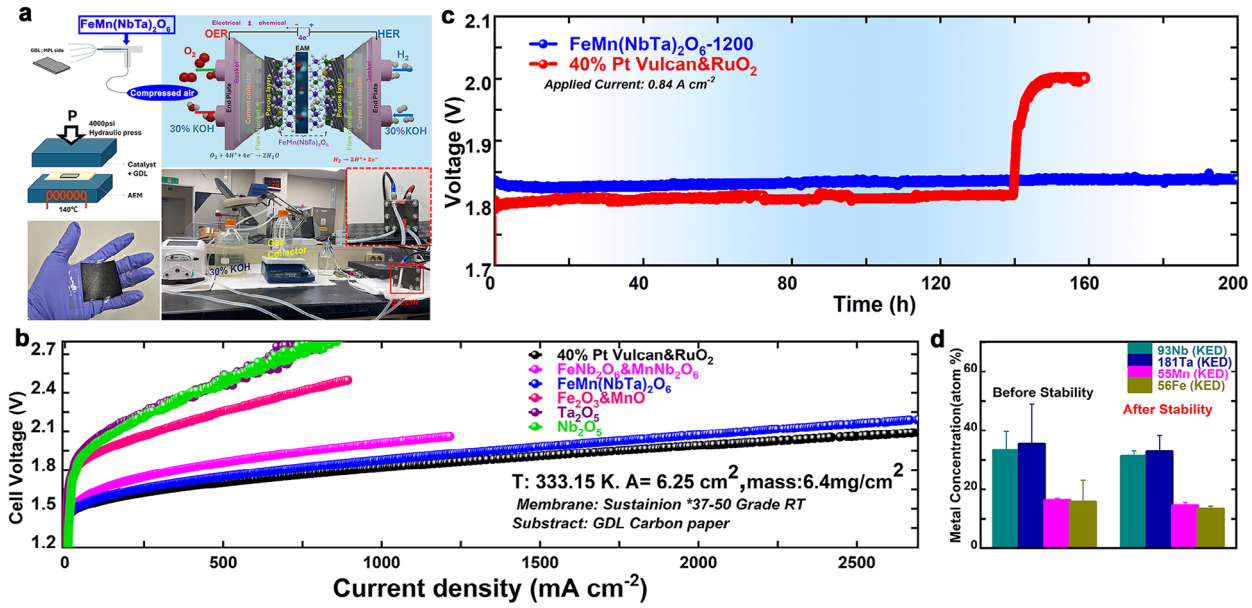

Figure 4. Performance and Stability of $FeMn(NbTa)_2O_6$ in an Anion Exchange Membrane Water Electrolyzer (AEMWE). a) Schematic illustration of electrode fabrication, showing $FeMn(NbTa)_2O_6$ ink spray-coated onto a gas diffusion layer (GDL) substrate and its integration into a single Anion Exchange Membrane Water Electrolyzer (AEMWE). b) Polarization curves for an AEM electrolyzer using $FeMn(NbTa)_2O_6$, $FeNb_2O_6$-$MnNb_2O_6$, Fe_2O_3-MnO, Nb_2O_5, Ta_2O_5, and 40% Pt/C-RuO_2 electrodes, conducted at a temperature of 333.15 K, with a 5 × 5 cm^2 cell area and a Sustainion 37–50 Grade RT membrane. c) Stability comparison of $FeMn(NbTa)_2O_6$ versus 40% Pt Vulcan-RuO_2 at a current density of 840 mA/cm^2, demonstrating long-term AEMWE performance. d) Elemental composition of the $FeMn(NbTa)_2O_6$ catalyst before and after the stability test.

electrode processes; this includes double-layer capacitance and charge transfer resistance.[39] θ reflects different interaction domains, including the strong interaction between electrode surfaces and complexes formed by catalyst active sites and OH, as well as the weak interactions in the low-frequency range corresponding to double-layer capacitance. In addition, the strong interaction between the electrode surfaces and catalyst-OH complexes can affect impedance behavior in the low-frequency range, leading to deviations from expected behavior for simple double-layer capacitors. This is because the strong interaction results in slower response times to applied sinusoidal perturbations for catalyst-OH complexes than for double-layer capacitance.

In addition, the slight decreases in the OER and HER polarization curves after 1000 CV cycles confirm the excellent electrocatalytic stability of $FeMn(NbTa)_2O_6$ (Figure 3g). The polarization curve of $FeMn(NbTa)_2O_6$ distinctly shows separate regions for HER and OER, with a clear onset potential for OER and a well-defined adsorption region for HER. In Figure 3h, the polarization curves of $FeMn(NbTa)_2O_6$ spray-coated on Nickel foam electrodes maintained their stability and activity at 0.2 A cm^{-2} in 20% KOH, namely compared to cell operation at 0.4 A cm^{-2} in 30% KOH. Here, high-concentration electrolytes induce mechanical stress on coatings during chromatoamperometry, resulting in a slight loss of active surface area and performance degradation.

2.3. Anion Exchange Membrane Water Electrolyzer Single-Cell Performance

To explore the applicability of columbite catalysts in alkaline water electrolysis, the $FeMn(NbTa)_2O_6$ catalysts were employed in the assembly of a single anion exchange membrane water electrolyzer (AEMWE). Their performance and durability were subsequently studied by connecting them to an electrolyzer testing system operating under the conditions of 30% KOH concentration, a temperature of 60 °C, and a Sustainion 37–50 Grade RT membrane, as illustrated in **Figure** 4a. The cell was prepared with $FeMn(NbTa)_2O_6$-based electrodes for both the cathode and anode, with gas diffusion layers (GDL) integrated into the stack as 5 × 5 cm^2 surface area units. Figure 4b shows the polarization analyses of $FeMn(NbTa)_2O_6$, $FeNb_2O_6$, and $MnNb_2O_6$ compared with the benchmark 40% Pt/C-RuO_2, as well as commercial materials such as Fe_2O_3-MnO, Nb_2O_5, and Ta_2O_5. Notably, $FeMn(NbTa)_2O_6$ exhibited a cell voltage of 1.81 V at a current density of 700 mA cm^{-2}, while $FeNb_2O_6$-$MnNb_2O_6$ showed a slightly higher cell voltage of ≈1.93 V at the same current density.

The performance of AEMWE tests with $FeMn(NbTa)_2O_6$ and $FeNb_2O_6$-$MnNb_2O_6$ was comparable to that of 40% Pt/C-RuO_2, which had a reduced cell voltage of 1.75 V. In contrast, Fe_2O_3-MnO, Nb_2O_5, and Ta_2O_5 demonstrated higher respective cell voltages of 2.38, 2.65, and 2.70 V under similar conditions. Stability testing at an applied current of 0.84 A cm^{-2} also confirmed the outstanding stable performance of the cells during 200 h in Figure 4c. The $FeMn(NbTa)_2O_6$ catalyst cell voltage remains nearly constant at ≈1.85 V, whereas the 40% Pt Vulcan-RuO_2 did not. To evaluate the chemical stability of $FeMn(NbTa)_2O_6$ under these conditions, we measured the metal concentrations before and after stability testing using inductively coupled plasma mass spectrometry (ICP-MS). As illustrated in Figure 4d, following the AEMWE stability test at a constant current density of 0.8 A cm^{-2}, the dissolution of Nb, Ta, Mn, and Fe was observed to be less than 5%. The dissolution of the A-site elements (Fe, Mn)

from $FeMn(NbTa)_2O_6$ was significantly lower compared to pre-stability test levels. These results indicate that the structure of the $FeMn(NbTa)_2O_6$ material remained unchanged after prolonged cell operation, with Nb and Ta centers playing a critical role in preventing the dissolution of Fe and Mn. This stability is essential for maintaining high catalytic activity in AEMWE processes.

2.4. In Situ Characterization to Identify Redox Activity

To understand the metal-center mediated mechanisms in adsorption and redox reactions for $FeMn(NbTa)_2O_6$ and $FeNb_2O_6$-columbite catalysts, in situ XAS was conducted. This allowed us to understand the evolution of local coordination environments and oxidation states at current densities (OCP, −10, −20 to 20 mA cm^{-2}) relevant to the HER and OER in both air and 1M KOH electrolyte, as illustrated in Figure S36, Supporting Information. The in situ Fe *K*-edge XANES spectra of $FeMn(NbTa)_2O_6$ (**Figure 5a**) and $FeNb_2O_6$ (Figure 5b) revealed variations in spectral edges shifting them toward higher energies, accompanied by broadening of white line peaks. These changes indicate significant variations in the chemical environments around Fe atoms. Conversely, the Fe *K*-edge XANES spectra of $FeNb_2O_6$ showed large differences in pre-edge intensities, indicating how the oxidation state of Fe transitions from its initial lower value (Figure S37a, Supporting Information) to higher values upon equilibration of the open circuit potential (OCP). As $J_{10mA/cm2}$ (E = 1.53 V vs. RHE) is applied to $FeNb_2O_6$ and $J_{20mA/cm2}$ (E = 1.51 V vs. RHE) to $FeMn(NbTa)_2O_6$, the pre-edge intensity moves down (regeneration) from the open circuit potential toward lower energies, namely when compared to the ex situ XANES of the Fe *K*-edge in $FeNb_2O_6$ (purple line) and $FeMn(NbTa)_2O_6$ (black line). During this redox process, Fe returns to its original valence state after removing electrons from O_2^- centers present in OH^- or H_2O, preventing higher Fe oxidation states from forming. Similarly, at current densities of $J_{-10mA/cm2}$ (E = −0.18 V vs. RHE) for $FeNb_2O_6$ and $J_{-20mA/cm2}$ (E = −0.16 V vs. RHE) for $FeMn(NbTa)_2O_6$, the pre-edge intensity at 7115 eV moves down from its initial state. This indicates a diminished Fe oxidation state upon oxidation via $Fe^{2+}\ O_6 \rightarrow Fe^{3+}\ O + e^-$, implying a parallel reduction pathway and multi-electron charge transfer involving Fe metal centers.[40] While applying negative current (E = −0.16 V vs. RHE) to the Fe *K*-edge of $FeMn(NbTa)_2O_6$, edge positions shift intensely to lower energies. This indicates a strong reduction of electrons transferred from oxygen species adsorbed on Fe^{3+}, namely toward O adsorbed to Fe in $FeMn(NbTa)_2O_6$ ex situ, at lower applied currents.[41] Furthermore, in situ Nb *K*-edge XANES spectra measurements were performed for $FeNb_2O_6$, and $FeMn(NbTa)_2O_6$ at the OCP, $j_{10\ mA\ cm-2}$, and $j_{-10\ mA\ cm-2}$. In Nb *K*-edge spectra, changes in Nb oxidation state are not frequently observed with applied current at the adsorption edge. Further, Nb *K*-edge XANES spectra in $FeNb_2O_6$ and $FeMn(NbTa)_2O_6$ (Figure S37b–d, Supporting Information) have line shapes resembling those of commercial Nb_2O_5. Although significant changes in Nb and Ta edges were not observed, this does not rule out Nb involvement in site activation. Interestingly, Nb *K*-edge adsorption evolved downward from $FeNb_2O_6$ and $FeMn(NbTa)_2O_6$ ex situ toward that of Nb_2O_5 at $J_{10mA/cm2}$ (E = 1.53 V vs. RHE), noting that these Nb exhibit high valence states of 5^+. The sharpened white-line peaks formed during the application of current suggest less distorted Nb–O coordination environments, indicating notable changes in local B-O bond coordination under the influence of applied current.[42] In the main edge, a more significant intensity change during redox activity was confirmed for Nb in $FeNb_2O_6$. Contrastingly, the energetic positions of line shapes for Ta L_3-edges in ex situ $FeMn(NbTa)_2O_6$, as shown in Figure 5c, resemble those of Ta_2O_5 reported elsewhere.[43] At the OCP, white lines gradually reduced to lower intensities, while at $J_{-10mA/cm2}$ (E = −0.128 V vs. RHE), white lines slightly moved up toward their initial states. Nevertheless, at $J_{10mA/cm2}$ (E = 1.53 V vs. RHE), the sharpened white lines blue shifted (Figure S37e,f, Supporting Information) from lower to higher energies while peak intensities decreased, indicating Ta coordination environments changed from being symmetric to asymmetric during the application of current. Also, redox behavior was observed through wavelet transforms of k_3-weighted Fe and Nb *K*-edge FT for $FeNb_2O_6$.

To unravel the intricate relationship between electronic structures and the observed in situ XANES phenomena, DFT-predicted projected density of states (DOS) results provided a comprehensive understanding of the impact of transition metals in AB_2O_6 electrocatalysts. The specific element site occupancy in the $FeMn(TaNb)_2O_6$ for the DFT calculations was determined from the parent $FeNb_2O_6$ material (Figure S38a, Supporting Information), which has a total of 36 atoms in the unit cell (consisting of 4 Fe, 8 Nb, and 24 O atoms). As Fe and Mn are expected to occupy the A site while Ta and Nb share the B-site, DFT calculations were carried out for different possible cation distributions (site occupancies) to determine the lowest energy configuration as shown in Figure S38b(b–e). Considering a layer-by-layer distribution of Fe and Nb in the parent material $FeNb_2O_6$, the first intuitive possible distribution of Fe, Mn, Nb, and Ta elements in $FeMn(TaNb)_2O_6$ is layer-by-layer (Model-1, Figure S38b, Supporting Information). Compared to the layer-by-layer ordering of each atom, we have also considered configurations in which there is a mixing of the two A-site elements (Fe and Mn) or B-site elements Nb and Ta) in the same layer. Model-2 considers mixing Nb and Ta in a layer (Figure S38c, Supporting Information) while keeping Fe and Mn in a layered order as in Model-1. Conversely, Model-3 considers mixing Fe and Mn in a layer (Figure S38d, Supporting Information) while keeping Nb and Ta in a layered order as in Model-1. Finally, Model-4 considers mixing Nb and Ta as well as mixing Fe and Mn in the same layer (Figure S38e, Supporting Information). Our DFT geometry optimization and energy minimization results show that Model-3 is energetically more favorable than Model-1 by 0.17 eV and Model-2 by 0.12 eV. Model-2 is found to be in a higher energy (+0.07 eV) state than Model-1. Analysis of the projected density of states (PDOS) from our previous study revealed that the introduction of Mn in AB_2O_6 resulted in the emergence of states at the valence band edge, while Nb incorporation introduced states at the conduction band edge.[9] Furthermore, the band gap exhibited narrowing with the inclusion of both Mn and Nb, indicating enhanced electrical conductivity in the doped material. This alignment with a lower overpotential suggests improved OER performance for $Fe_{0.75}Mn_{0.25}Ta_{1.875}Nb_{0.125}O_6$ versus pure $FeTa_2O_6$. In the present study, compared to the bimetallic $FeTa_2O_6$, $FeNb_2O_6$, $MnTa_2O_6$,

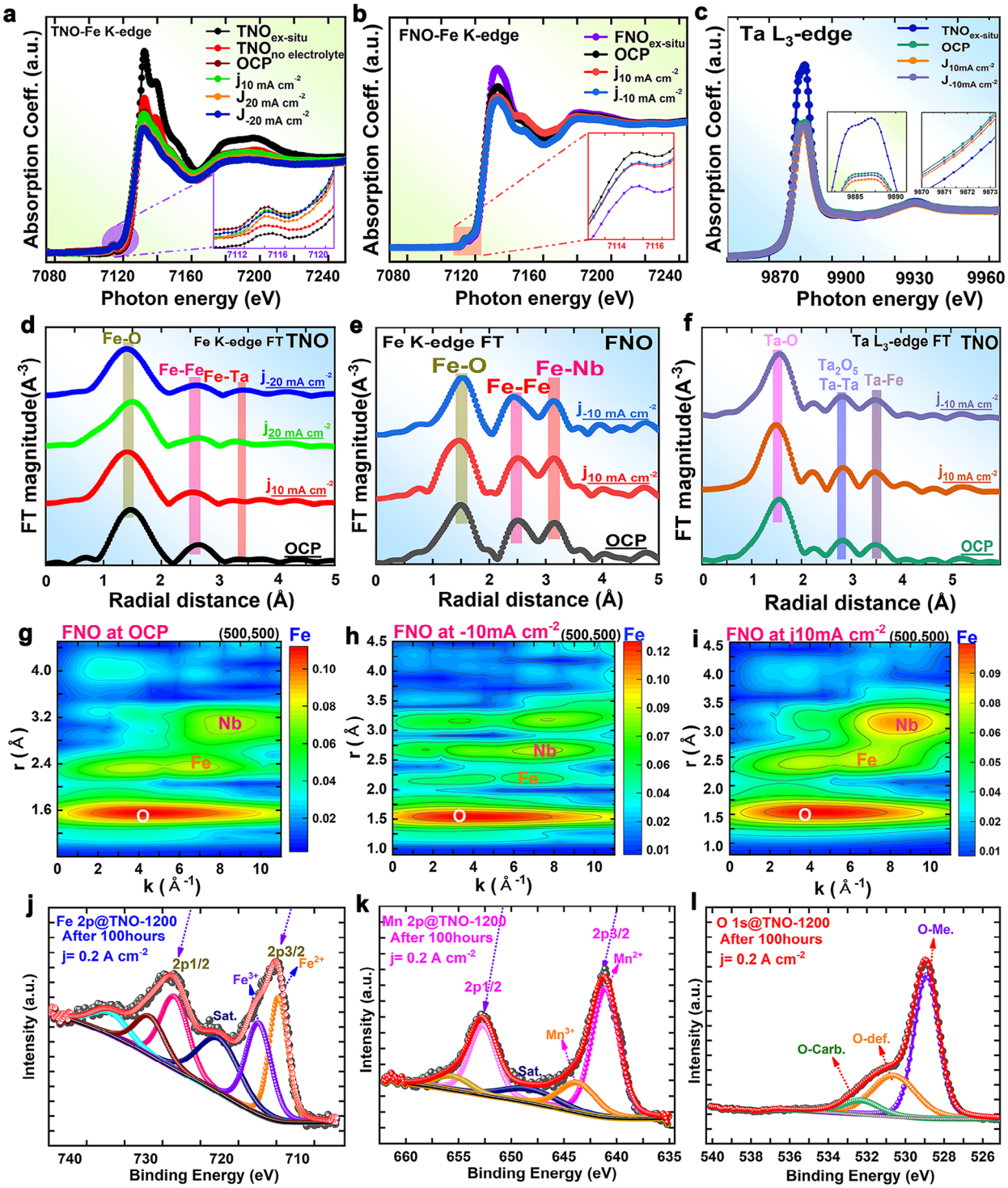

Figure 5. In situ Characterization of Redox Activity via X-Ray Absorption Spectroscopy (XAS). a) In situ Fe K-edge XANES spectra for $FeMn(NbTa)_2O_6$ (TNO) measured at Open Circuit Potential (OCP), and current densities of J = 10 mA cm^{-2}, J = 20 mA cm^{-2}, and J = −20 mA cm^{-2}, compared with ex situ measurements in air. b) In situ Fe K-edge XANES spectra for $FeNb_2O_6$ (FNO) at OCP, J = 10 mA cm^{-2}, and J = −10 mA cm^{-2}, compared with ex situ conditions. c) Operando Ta L_3-edge XANES spectra for $FeMn(NbTa)_2O_6$, showing spectral variations under OCP, J = 10 mA cm^{-2}, and J = −10 mA cm^{-2} conditions. d) FT-EXAFS spectra for the Fe K-edge in TNO, showing Fe-O, Fe-Fe, and Fe-Ta bond distances under different conditions. e) FT-EXAFS spectra for the Fe K-edge in FNO, showing variations in Fe-O and Fe-Nb bonds. f) FT-EXAFS spectra for the Ta L_3-edge in TNO, indicating Ta-O and Ta-Ta bond environments under varying electrochemical conditions. g-i) In situ wavelet transform (WT) analyses of Fe K-edge and Nb K-edge for FNO, showing coordination changes and bond variations at OCP, J = −10 mA cm^{-2}, and J = 10 mA cm^{-2}. j–l) High-resolution XPS of Fe 2p, Mn 2p, and O 1s regions for $FeMn(NbTa)_2O_6$ after 100 h of electrochemical stability testing at J = 0.2 A cm^{-2}.

and $MnNb_2O_6$ (Figure S39a–d, Supporting Information) materials, the multimetallic $FeMn(TaNb)_2O_6$ exhibited a significantly reduced band gap. This reduction, coupled with gap states primarily arising from Fe and Mn, facilitates the transfer of electrons from the valence band to the conduction band, enhancing electrical conductivity. Such improved conductivity is highly desirable for achieving efficient H_2O/H_2 redox coupling.

In situ Fourier-transformed extended X-ray adsorption fine structure (FT-EXAFS) analyses of FNO and $FeMn(TaNb)_2O_6$ reveal changes in their local structures and coordination environments with variations in applied current densities. These changes are evident in the primary peaks attributed to single scattering paths. These correspond first to the nearest A–O peaks, followed by A–A and A–B peaks observed in $FeNb_2O_6$ and $FeMn(TaNb)_2O_6$ for Fe, Nb, and Ta edges. For $FeNb_2O_6$ ex situ Fe *K*-edge FT spectra results in Figure 5e and Figure S40, Supporting Information, coordination numbers (CN) reduced from 5.5 to 4 for Fe-O pathways compared with the spectrum at OCP, while interatomic distances stretched from d = 1.94–1.97 Å. When the current was set to $j_{10mA/cm2}$ (E = 1.53 V vs. RHE), Fe-O pathways in $FeNb_2O_6$ (Table S6, Supporting Information) showed slight upshifting in coordination numbers, reaching 4.3 without significant changes in bond lengths. However, at J = −10 mA cm^{-2} (E = −0.18 V vs. RHE), the Fe-O bond length gradually increased to 1.98 Å, and coordination numbers slowly decreased to 3.8. Similarly, Fe *K*-edge FT analysis results for $FeMn(TaNb)_2O_6$ (Figure 5d, Table S7, Supporting Information) showed the same behavior, in which coordination numbers were exactly 6 initially. After increasing the current, CN became less than 6 (Figure S41b, Supporting Information), while interatomic distances did not significantly change. These results indicate an ongoing geometric conversion from octahedral to tetrahedral coordination during the redox process.[44] Additionally, as shown in Table S8, Supporting Information, *R*-space fitting results of Fe and Nb *K*-edges reveal that Fe and Nb atoms in $FeNb_2O_6$ at applied currents show that Fe *K*-edges at OCP exhibited coordination numbers in studied paths equal to 4.2 for Nb-Nb, 3.3 for Fe-Fe, and 5.0 for Fe-Nb. When applying J = −10 mA cm^{-2} (HER step), Fe-O1 coordination reduced to 3.8 (d = 2.01 Å), Fe-Fe to 3.2 (d = 2.94 Å), and Fe-Nb to 3.51 (d = 3.51 Å), given influence from the breaking of OH–H bonds. Subsequently, at $J_{10mA/cm2}$ (OER step), coordination numbers were re-established to 4.2 for Fe-O, 3.7 for Fe-Fe, and 5.0 for Fe-Nb. Respective sunlight scattering paths of 2.02 Å, 2.93 Å, and 3.51 Å were observed for Fe-O, Fe-Fe, and Fe-Nb paths.

Additionally, in Table S8, Supporting Information, in situ Nb *K*-edge FT fitting results illustrate that at the open circuit potential (OCP), Nb-O paths exhibit localization at distances of 1.91–2.11 Å, Nb-Fe paths at 3.23 Å, and Nb-Nb paths at 3.68 Å. In our previous work, we clarified that the higher Nb–O distances extend to 2.3 Å in the pristine state, while Nb–Fe and *b-c* coplanar Nb-Nb pairs respectively have bond lengths of 2.82 Å and 3.23 Å.[9] Upon increasing the current to $J_{10mA/cm2}$, Nb-O pathways slightly changed while their coordination numbers remained at 6. In contrast, applying $J_{-10mA/cm2}$ (E = −0.18 V vs. RHE) to $FeNb_2O_6$ did not change Nb-O bond distances, though their coordination numbers were reduced to 5. In other words, the coordination number can change without much modification of bond distances. Regarding Nb-Fe and Nb–Nb pairs in the *b-c* plane at $J_{10mA/cm2}$, we can observe in Table S9, Supporting Information that distances were increased from 2.82 to 3.21 Å for Nb-Fe – and from 3.23 to 3.71 Å for Nb-Nb – in $FeNb_2O_6$. Contrastingly, Nb-Fe and Nb–Nb distances gradually reduced at J = −10mA cm^{-2}. Their distances were close to those observed in OCP, indicating degeneration. Meanwhile, disorder factors deduced from Debye-Waller factors (σ^2, Å^2) did not exhibit much change during increases in applied potential (Figure S41c,d, Supporting Information). This suggests relative stability in the structural disorder of materials. The observation of these increases in distances between Nb-Fe and Nb–Nb pairs in *b-c* planes at a current of $J_{10mA/cm2}$ suggests a possible reduction in the valence of niobium (Nb), and an attenuation of the Jahn–Teller effect within $FeNb_2O_6$ under the influence of applied current.

Moreover, the Ta L_3-edge FT analysis results of $FeMn(NbTa)_2O_6$ (Figure 5f, Figure S42, and Table S10, Supporting Information) were consistent with Ta L_3-edge XANES. From the OCP to J = −10 mA cm^{-2}, the coordination number reduced from 5.9 to 4.9 while Ta-O bond distances stayed stable. At 10 mA cm^{-2}, coordination numbers of Ta-O paths were reduced to 5.3 with upshifting when reaching equilibrium (OCP), indicating a reverse evolution. This can be attributed to notable modifications in Ta-O paths during redox reactions, leading to substantial electronic redistributions along these pathways.[14b,45]

Furthermore, the wave transforms (WT) in Figure 5g–i show that M-O WT signals are localized above 3 Å (R-space) and 10 Å^{-1}(k-space). This suggests specific spatial arrangements exist in relation to metal-oxygen interactions, potentially influencing adsorption and redox reactions. Consistent with the stacking arrangements and defects observed in Figure S41g, Supporting Information, the RGB-high-magnification HAADF–STEM image taken after electrochemical stability testing also indicates how structural layers change in stacking arrangements, exhibiting different point defects in crystal lattices of $FeMn(NbTa)_2O_6$ to substantiate geometric alternation.[46] Contour plots at OCP, $J_{10mA/cm2}$, and $J_{-10mA/cm2}$ provided much more significant resolution of located structures in both *k*-space and *R*-space. The high-resolution x-ray photoelectron spectroscopy of Fe 2*p*, Mn 2*p*, and O 1*s* (j = 0.2 A cm^{-2}) in Figure 5j–l, Supporting Information, taken after electrochemical studies, show that original $2p_{3/2}$ and $2p_{1/2}$ peaks shifted and exhibited multiple oxidation states (2+/3+) at A-sites. In addition, O 1*s* peaks were fitted to three oxygen-based signals, namely O-methane at ≈529 eV, O-defect at ≈531 eV, and O-C at ≈533 eV. These are associated with surface-adsorbed H_2O molecules coupled with organic carbon.[47]

2.5. Origins of Electron Transfer Mechanisms in the $FeMn(NbTa)_2O_6$ Catalyst

In Figure S43a,b, Supporting Information, the isosurfaces of charge for AB_2O_6-columbite structures are plotted at levels of 0.48 and 0.83 e Å^{-3}, indicating cation sites and other volumetric components of simulated cells that have a charge value equal to or greater than that of a threshold level. At lower isosurface levels, Mn, Fe, and O have distinguishably higher charge densities than other volumetric cell components, while only Fe and O remain discernibly more charged at higher isosurface levels. This result indicates that Fe and Mn are uniquely responsible for localizing

charge in their bonds with O, thereby inhibiting charge transfer to adsorbing species (OH*, O*, and OOH*) on $FeMn(NbTa)_2O_6$-columbite surface. This implies charge transfer to adsorbates is less for A-site than B-site cations. Different iso-surface level results particularly emphasize this charge transfer uniqueness and further lessened magnitude for Fe.

As shown for atom-projected densities of states (PDOS) in **Figure 6a**, the electronic structures of individual representative Fe, Mn, Ta, and Nb cations, accompanied by corresponding adjacent O atoms, depict orbital hybridization and electronic interactions between such A-O and B-O atom pairs. The lower valence bands and higher conduction bands (Figure S44, Supporting Information) far from the Fermi energy (E_F) are consistent over all cation-O pairs. However, the partial delocalization of electrons near E_F, induced by partial orbital filling of t_{2g} and e_g bonding (Figure S45, Supporting Information) energy levels in higher valence bands and corresponding t_{2g}* and e_g* anti-bonding orbitals in lower conduction bands, distinguish metal centers from each other. Relative to the energy level gap between the conduction and valence energy bands observed across all cations, there exists intermediate t_{2g} and e_g band gap states unique to each metal center. These metal centers have characteristic 3*d* (Mn, Fe), 4*d* (Nb), or 5*d* (Ta) orbitals. Each cation develops three characteristic valence band PDOS peaks, which hybridize with overlapping O 2*p* orbital peaks to enable distinct charge transfer behaviors across A-O and B-O bonds. Enhanced charge transfer across cations and O implies the strengthening of corresponding cation-O bonds and thereby weakening of bonds with adsorbates.[48] Therefore, the conduction band edges of each cation, which begin on the rightward edges of the band gaps following valence *d*-band peaks, feature (less) distinct charge transfer behaviors. Given the low partial filling of valence *d*-orbitals, Nb and Ta both feature three small and delocalized t_{2g} and e_g valence band edge peaks, which have similar or slightly larger magnitudes than their respective hybridized O 2*p* orbitals. Both conduction band edges initially slowly increase with respect to their overlapping O 2*p* orbitals, forming shallow conduction band edges, though Nb subsequently improves more quickly than Ta at higher conduction band levels. Overall, these results indicate relatively weak overall charge transfer and bonding between Nb/Ta and O bonds, consistent with plotted charge densities. This enables greater charge transfer with adsorbates, and thereby likely stronger bonding and more favorable adsorption energies. In contrast, Mn features a shallow intermediate t_{2g}/e_g band peak, two strong corresponding leftward and rightward valence band peaks, and a relatively shallow (slowly increasing) conduction band edge. Following ligand field theory, this indicates that the hybridized orbital contribution to Mn-O bonding is weakest at a partially filled intermediate energy level. To achieve this, Mn (d^5) fills t_{2g} and e_g orbitals in a high-spin configuration, adding single electrons to single orbitals in the order given by its corresponding energy level diagram. Thus, partially filled intermediate energy levels or orbitals are possible. In contrast, Fe features its smallest peak at its rightmost t_{2g}/e_g orbital or valence band edge in Figure 6b, with matching lower Fe-O bond strength and charge transfer at this peak. The significance of this result is achieved by isolating out t_{2g} and e_g orbital contributions. Figure 6c illustrates that when decomposing t_{2g} and e_g orbital contributions from the whole *d*-band near the valence band edge, Mn, Nb, and Ta do not feature any distinct features versus their entire *d*-bands, such as missing peaks. As shown in Figure S46, Supporting Information, we examined e_g bonding and anti-bonding orbital filling results in M-O (M = Mn, Nb, and Ta) and Fe-O covalent bonds in $FeMn(NbTa)_2O_6$. Consequently, we observed a charge transfer between Fe-O along the x^2-y^2 and z^2 orbital directions, aligning with changes in Fe K pre-edge intensities during the application of current densities.

This phenomenon leads to further variation of structural geometry, enhancing the redox activity in Fe environments compared to M-O (M = Ta, Nb, and Mn) in $FeMn(NbTa)_2O_6$. This indicates that charge density becomes particularly concentrated on Fe, as fewer charge transfer mechanisms for Fe become available. The limited geometric availability of diverse electronic transfer mechanisms may also contribute to the strengthening or localization of existing Fe-O bonds, thereby further diminishing Fe-adsorbate charge transfer, bonding, and adsorption energies relative to Mn. However, Fe lacks its uppermost valence *d*-band peak, as shown in its decomposed e_g PDOS in Figure 6b. Therefore, the highest energy level for Fe must be e_g and it is (effectively) empty or unfilled. Thereby, little to no orbital hybridization, bonding, and charge transfer occurs between Fe and O along the x^2-y^2 and z^2 orbital directions.[49] To achieve this, Fe (d^6) would fill t_{2g} levels in a low-spin configuration, in which lower energy levels are filled with electrons until they are completely filled. Here, no partial filling occurs except for the highest energy level currently being filled. There are three t_{2g} orbitals that can hold six total electrons until e_g orbitals would be necessarily partially filled, thus a missing e_g orbital can only be observed by Fe (d^6) when all t_{2g} orbitals are filled in a low-spin configuration.

The t_{2g}-e_g splitting generally refers to t_{2g}* and e_g* anti-bonding orbital (Figure S47, Supporting Information) differences over energy (*x*-axis of PDOS). However, when comparing the PDOS of Fe with that of other cations, an effective splitting gap is formed between the conduction *d*-band and either the t_{2g} (Fe) or e_g (Mn, Ta, Nb) orbitals of the valence band. The difference in the element-specific band gap, induced by effectively removing the rightmost (e_g) valence band peak for Fe, is approximately 0.7 eV (gaps: Fe = 0.9 eV, Mn/Ta/Nb = 1.6 eV). Per the rule for the binding of adsorbate transition metals, the weaker charge transfer and bonding of Nb and Ta with oxygen allow for correspondingly stronger interactions with *OH and OOH adsorbates. This enhanced interaction results in more favorable adsorption energies for these intermediates.[50] In contrast, the very strong Fe-O charge transfer leads to weaker interactions with adsorbates, reducing adsorption energy. Moreover, the more delocalized *d*-orbital states of Mn, across t_{2g} and e_g orbitals, feature moderate charge transfer and bonding between oxygen and adsorbates. This is reflected in adsorption energies and charge transfer values (Δq), providing an optimal balance.

Figure 6d shows that charge transfer occurs first between hybridized metal-oxygen orbitals and t_{2g}/e_g bonding orbitals, then between t_{2g}/e_g bonding and anti-bonding orbitals. The geometry of possible charge transfer paths is determined by whether t_{2g} or e_g orbitals are filled. Given e_g orbitals cannot be filled for Fe, charge transfer occurring along x^2-y^2 and z^2 orbital directions cannot occur between Fe and O. This may explain why charge density is particularly concentrated on Fe, as fewer charge transfer mechanisms for Fe are available.[51] This lack of geometric availability of different electronic transfer mechanisms may also

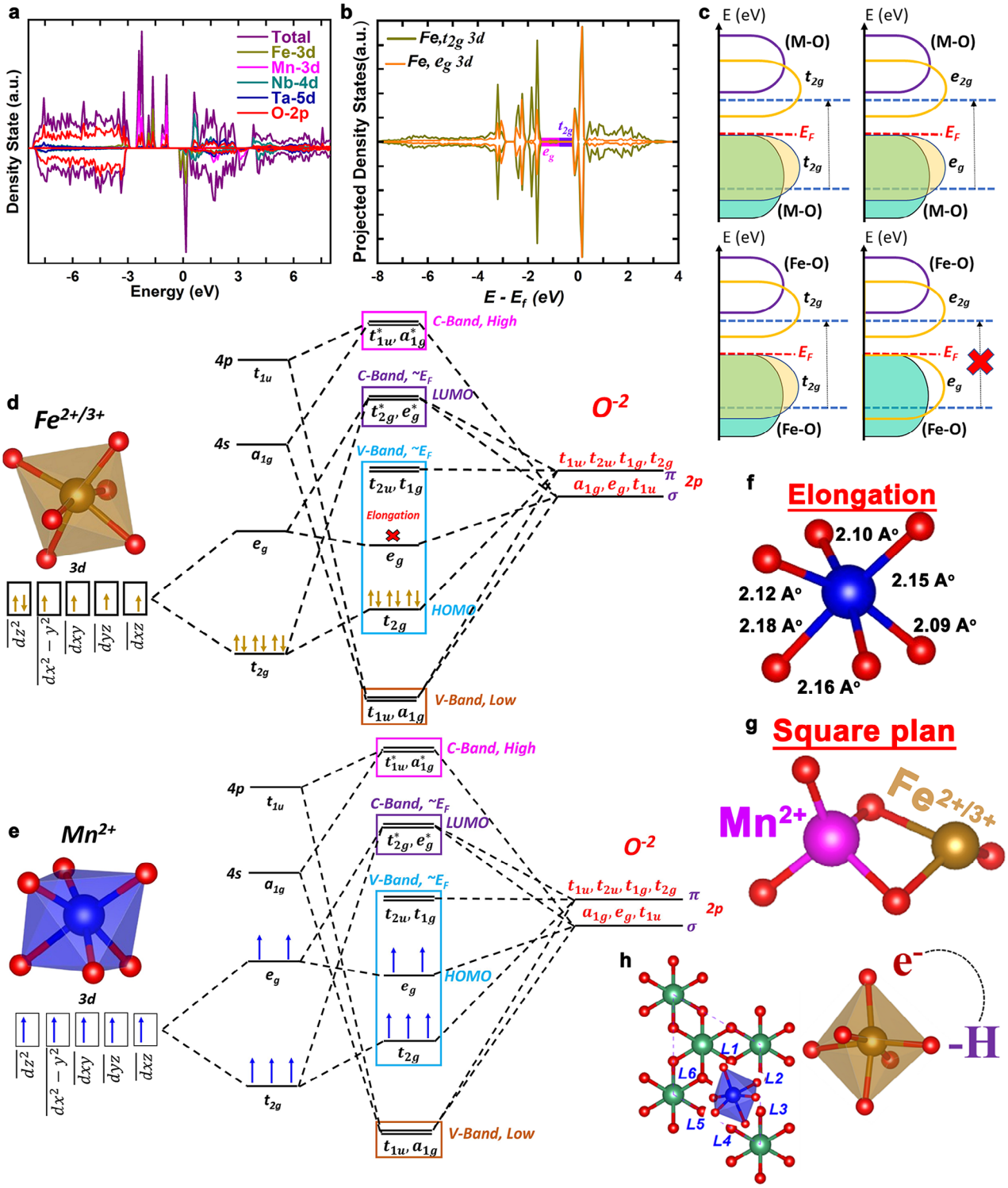

Figure 6. Electronic Structure and Local Geometry Analysis of Fe and Mn Sites in $FeMn(NbTa)_2O_6$ Materials. a) Total density of states (DOS) for Fe 3d, Mn 3d, Nb 4d, Ta 5d, and O 2p orbitals, showing contributions to the electronic structure. b) Projected density of states (PDOS) for Fe showing t_{2g}-e_g orbital near the Fermi level relevant to charge transfer. c) Schematic energy level diagrams showing the electronic configuration of metal-oxygen (M-O (M = Mn, Nb, Ta)) and Fe-oxygen (Fe–O) bonds for different energy bands (C-band and V-band). d) Simplified ligand-field energy diagram of $Fe^{2+}/^{3+}$ sites within the octahedral geometry, illustrating elongation effects and t_{2g} orbital filling. e) Mn^{2+} electronic structure in octahedral coordination, highlighting spin alignment and orbital energy levels. f) Local bond elongation and coordination geometry for MO_6 octahedra, showing bond lengths between M and surrounding oxygen atoms. g) Square planar coordination environment of Mn^{2+} and $Fe^{2+}/^{3+}$ ligand stabilization effects. h) Illustration of ligand stabilization of MnOOH species and initial H_2O adsorption on Fe sites.

further strengthen or localize existing Fe-O bonds, thereby further weakening Fe-adsorbate charge transfer, bonding, and adsorption energies relative to Mn in Figure 6e. This geometric charge transfer inhibition is accompanied by the corresponding asymmetry or radial distortion in the FeO_6 octahedron, which further relatively localizes charge to square planar FeO_4 bonding (Jahn-Teller-like distortion).[52] This inhibition of geometric charge transfer is accompanied by a corresponding asymmetry or radial distortion in the FeO_6 octahedron, as illustrated in Figure 6f,g, further localizing charge to square planar FeO_4 bonding.[53] This further localization of charge can justify the slightly worse charge transfer and bonding of Fe to adsorbates versus Mn.[54] Moreover, as illustrated in Figure 6h, the metal-oxygen coordination in FeO_6 and FeO_4 significantly alters the electronic environment around the metal centers. This modification impacts the distribution of electron density, and the effective nuclear charge experienced by the hydrogen atoms.[55] For instance, the ligands surrounding A-sites may increase electron density around these metals, leading to positive adsorption energies due to repulsion between the electron-rich metal centers and hydrogen.[56] In contrast, Nb and Ta exhibit more dispersed electron densities due to their *d*-orbital interactions with oxygen ligands, thereby lowering the energy barriers for hydrogen adsorption and stabilizing related interactions.[57] The coexistence of 3*d*, 4*d*, and 5*d* metal centers in tantalite-columbite, combined with modified octahedral geometry and electronic structure, demonstrate increases in electrical conductivity. Such improvements in electronic conductivity can be linked to atomically localized differences in electronic transfer capabilities across various columbite and tantalite cations. Large differences in *d*-band filling at valence band edges near the Fermi level necessarily exist between columbite-tantalite *A*-sites (Mn and Fe, 3*d*) and *B*-sites (Nb, 4*d* and Ta, 5*d*), considering their strongly different electronic configurations.[58] The lower *d*-orbital occupation of Nb and Ta (d^3) prevents strong metal-oxygen bonding with bulk and surface O from columbite-tantalite, which would be facilitated by significant *d-p* orbital hybridization near the valence band edge. In contrast, Mn (d^5) and Fe (d^6) feature stronger corresponding 3*d* metal and O 2*p* orbital overlap. Considering electronic structure principles and *d*-band theory,[59] weakened Nb-O and Ta-O bonding favors adsorbate binding over that observed for Mn-O and Fe-O. Within Mn and Fe, more nuanced energetic differences arise from the geometrically distinct *d*-band filling corresponding to Jahn-Teller-like distortions of AO_6 octahedral shells.[60] The interplay of spin configuration and t_{2g} versus e_g orbital occupation differences renders Fe with more square planar AO_4 character than Mn, further strengthening its bonding with columbite-tantalite O along the *x*, *y*, and *z* planes while weakening it along the radial z^2 and x^2-y^2 directions.[61] These geometric distinctions more subtly affect reactant binding with OH^- ions in combination during the lattice oxygen oxidation mechanism (LOM). For example, $Fe^{2+}O_6$ is first oxidized to Fe-OOH (Fe^{3+}). In the next step, when OH^- ions in solution attack Fe-OOH and H^+ is removed, Fe-OOH is converted into Fe-OO, and then O_2 is oxidized and desorbed.[62]

To elucidate the reaction pathways and intermediates involved in the oxygen evolution reaction (OER) on $FeMn(NbTa)_2O_6$ and its derivatives ($FeNb_2O_6$, $MnNb_2O_6$, $FeTa_2O_6$, and $MnTa_2O_6$), first-principles Hubbard-corrected density functional theory (DFT+U) calculations were employed. The adsorption energies (E_{ads}) of key intermediates (OH*, O*, and OOH*) and the corresponding rate-determining steps (RDS) were analyzed for Fe, Mn, Nb, and Ta active sites. Solvation effect is crucial for the accurate prediction of the OER intermediates adsorption (*O, *OH, and *OOH), as the solvent molecules may interact with the adsorbed species and impact the energetics. Thus, the solvation effect is included by the implicit electrolyte model implemented in VASPsol with a Debye length of 3.0 Å, which corresponds to a 1 M ionic concentration and a dielectric constant of 78.4 for the aqueous solution.[63] The solvation energy is defined by ΔE_{sol} (eV) = $E_{solv} - E_{gas}$, where E_{solv} and E_{gas} are the total energy of the system with and without solvation included, respectively. Single-point calculations were carried out to include the solvent effect. By this definition, a more negative solvation energy implies higher stabilization of the species due to solvation. The results revealed distinct catalytic roles for A-sites and B-sites, driven by differences in adsorption energetics and charge transfer.

At the $FeMn(NbTa)_2O_6(010)$ surface, the solvation-corrected adsorption energies (Figure S48, Table S11, Supporting Information) of OH*, O*, and OOH* at the A-sites were calculated to be −3.69, −2.16, and −2.39 eV at Fe sites, and −3.66, −2.37, and −2.48 eV at Mn sites, respectively. At B-sites, the adsorption energies were significantly stronger: −5.17, −4.50, and −3.21 eV at Nb sites, and −4.38, −3.85, and −2.91 eV at Ta sites. These trends were consistent across the single-component catalysts. For instance, on $FeNb_2O_6(010)$, the solvated adsorption energies ($E_{ads\text{-}sol}$) for OH*, O*, and OOH* were −3.63, −1.95, and −2.58 eV at Fe sites, and −4.42, −3.53, and −3.08 eV at Nb sites (Figure S49, Table S11, Supporting Information). Similarly, for $FeTa_2O_6(010)$ (Figure S50, Table S11, Supporting Information), Fe sites exhibited $E_{ads\text{-}sol}$ values of −3.56 (OH*), −1.85 (O*), and −2.74 eV (OOH*), whereas the Ta sites displayed stronger adsorption of −4.86 (OH*), −3.95 (O*), and −3.27 eV (OOH*). For $MnNb_2O_6$ (010) (Figure S51, Table S11, Supporting Information), the Mn sites exhibited adsorption energies of −3.63 (OH*), −2.32 (O*), and −2.61 eV (OOH*), while the Nb sites showed stronger binding with −5.10 (OH*), −3.89 (O*), and −3.21 eV (OOH*). Similarly, on $MnTa_2O_6$ (010) (Figure S52, Table S11, Supporting Information), OH*, O*, and OOH* adsorbed at −3.49, −2.37, and −2.70 eV on Mn sites, and at −4.77, −3.83, and −3.13 eV on Ta sites, respectively. This consistent pattern indicates that Nb and Ta share a tendency for stronger stabilization of intermediates (OH* and OOH*), whereas Fe and Mn exhibit moderate binding energies, favoring redox activity and turnover of O*. This difference is particularly evident in mixed systems like $FeMn(NbTa)_2O_6$, where Nb and Ta contribute by strongly anchoring intermediates, ensuring structural stability, and enhancing the reaction environment. In contrast, Fe and Mn facilitate the formation and desorption of O*, the key intermediate for oxygen evolution. Table S11, Supporting Information summarizes the adsorption energy of O*, OH*, OOH* intermediates with and without the inclusion of solvation effects. We find that solvent strongly stabilizes O* by 0.40–0.55 eV, whereas OH* is stabilized by 0.21–0.29 eV, and OOH* is stabilized by 0.31–0.39 eV on the different cation sites at $FeMn(NbTa)_2O_6$ columbite materials surface. The more negative adsorption energies with the additions of solvents indicate that solvation strengthens the bonds between adsorbates and the surface. These results are

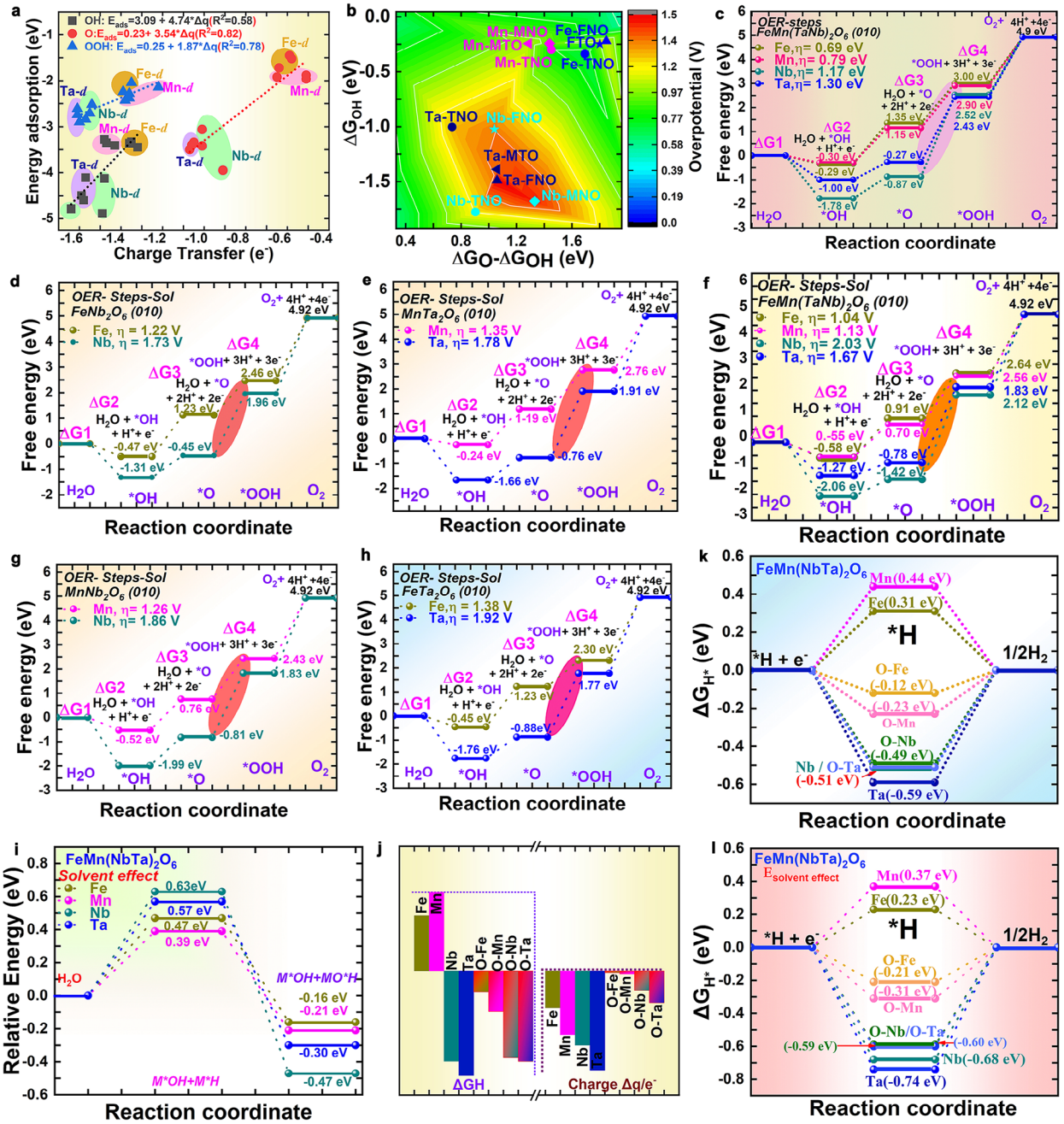

Figure 7. Adsorption and Redox Reactions Pathways. a) Correlation between adsorption energies (E_{ads}) and charge transfer (Δq) of metal centers. b) Calculated 2D Volcano plot of OER Overpotential (η) with ΔG_{OH} and ΔG_O-ΔG_{OH}. c) Four-electron mechanism of OER intermediates (*O, *OH, and *OOH) and free energy changes on $FeMn(NbTa)_2O_6$ surfaces at $U = 0$ V. d–h) OER Solvent-effects on $FeNb_2O_6$, $MnTa_2O_6$, $FeNb(NbTa)_2O_6$, $MnNb_2O_6$ and $FeTa_2O_6$ surfaces. i) Relative energy of H_2O adsorption with corresponding transition states (TS), dissociation and H_2O splitting on Fe, Mn, Nb, and Ta of $FeMn(NbTa)_2O_6$. j) Relationship between computed ΔG_{H*} values and evaluated Bader charges on Fe, Mn, Nb, Ta, and O surfaces. K,l) Gibbs free energies of hydrogen adsorption (ΔG_{H*}) on Mn, Fe, O-Fe, O-Mn, O-Nb, Nb, O-Ta, and Ta of $FeMn(NbTa)_2O_6$ with and without solvent.

consistent with theoretical results obtained on Pt(111), where a stronger stabilization effect is obtained with solvation.[64]

Figure 7a demonstrates a linear correlation between the adsorption energies of OH*, O*, and OOH* and the charge transfer (Δq) of metal centers (Fe, Mn, Nb, and Ta). Here, adsorption energy increases as electron transfer (Δq) becomes more negative. The slopes of these linear trends indicate that Fe and Mn sites, associated with AO_6 centers, exhibit lower charge transfer (Δq) values (−1.32 and −1.43 e^-, respectively), corresponding to weaker adsorption of intermediates. Conversely, Nb and Ta at BO_6 centers exhibit higher charge transfer (Δq: −1.49 $e^-$for Nb, −1.57 $e^-$for Ta), leading to stronger adsorption of intermediates,

especially OH* and OOH*. These linear relationships are expressed as:

OH*	$E_{ads} = 3.09 + 4.74\Delta q$ ($R^2 = 0.58$)
O*	$E_{ads} = 0.23 + 3.54\Delta q$ ($R^2 = 0.82$)
OOH*	$E_{ads} = 0.25 + 1.87\Delta q$ ($R^2 = 0.78$)

Each slope indicates a correlation between electron transfer and the adsorption energy of the molecule following equations described by Nørskov, where:

$$H_2O \rightarrow HO^* + H_2O + H^+ + e^-$$
$$Fe_{\Delta q} = -1.32e^-,\ Mn_{\Delta q} = -1.43e^-,\ Nb_{\Delta q} = -1.49e^-,\ Ta_{\Delta q} = -1.57e^-$$
$$\rightarrow O^* + H_2O + 2H^+ + 2e^-,$$
$$Fe_{\Delta q} = -0.64e^-,\ Mn_{\Delta q} = -0.65e^-,\ Nb_{\Delta q} = -0.91e^-,\ Ta_{\Delta q} = -1.05e^-$$
$$\rightarrow HOO^* + 3H^+ + 3e^-\mathrm{r}$$
$$(Fe_{\Delta q} = -1.35e^-,\ Mn_{\Delta q} = -1.22e^-,\ Nb_{\Delta q} = -1.54e^-,\ Ta_{\Delta q} = -1.61e^-)$$
$$\rightarrow O_2 + 4H^+ + 4e^-$$

This allows adjustable adsorption of reactants on Fe, Mn, Nb, and Ta metal centers of $FeMn(NbTa)_2O_6(010)$ surfaces. These differences in charge transfer behavior underscore the localized charge density at Fe and Mn metal centers relative to the more delocalized charge transfer at Nb and Ta centers, which stabilize adsorption intermediates more effectively.[15] This greater charge localization at Fe and Mn metal centers accounts for the observed differences in adsorption energies and charge transfer behavior.[65]

Figure 7b depicts a volcano plot with two spatial dimensions mapping the relationship between Gibbs free energy differences ($\Delta G_{O*} - \Delta G_{OH*}$) and the overpotential for Fe, Mn, Nb, and Ta active sites. The contour map demonstrates that AO_6 sites occupy regions associated with lower overpotentials, consistent with their role as redox-active centers. In contrast, BO_6 sites exhibit higher overpotentials, which reflect their tendency to strongly stabilize OH* intermediates. The positioning of Fe and Mn at the low overpotential region correlates with their higher Gibbs free energy differentials (1.49 eV for Fe and 1.25 eV for Mn). Thus, they favor O* formation, which is critical for OER catalysis. Conversely, Nb (0.63 eV) and Ta (0.49 eV) exhibit stronger OH* stabilization. Overall, the additional consideration of solvation effects does not change the Gibbs free energy ordering of any cations per material. Further, the proportions of most free energy differentials across these cations are generally conserved between calculations treating or ignoring solvents. Rather, handling solvent effects largely uniformly shifts free energetic potentials upward, lowering the stability of adsorbed species.

As shown in Figure 7c, all four elementary reaction steps involved in the oxygen evolution reaction on $FeNb_2O_6$, $FeTa_2O_6$, $MnNb_2O_6$, $MnTa_2O_6$, and $FeMn(NbTa)_2O_6(010)$ surfaces are found to proceed uphill in free energy when no potential is applied (U = 0). To make all steps thermodynamically downhill, an additional potential must be applied, and the minimum theoretical η are determined to be 0.69 and 0.79 V for Fe and Mn active sites, respectively. These results demonstrate that the A-site metals exhibit superior catalytic activity for the OER compared to the B-site metals, which show higher overpotentials of 1.17 and 1.30 V, respectively. Figure S53, Supporting Information provides a schematic representation of the adsorption mechanisms at A-sites and B-sites. The OER occurred following the 4e-mechanism proposed by Norskov for water oxidation:[66]

$$* + H_2O \rightarrow HO* + \left(H^+ + e^-\right) \Delta GI \quad (2)$$

$$HO* \rightarrow O* + \left(H^+ + e^-\right) \Delta GII \quad (3)$$

$$O* + H_2O \rightarrow HOO* + \left(H^+ + e^-\right) \Delta GIII \quad (4)$$

$$HOO* \rightarrow * + O_2 + \left(H^+ + e^-\right) \Delta GIV \quad (5)$$

Previous studies on oxygen evolution reaction catalysts – such as FeCOTa, FeCONb, $Pb_2Ru_2O_{6.5}$ perovskites, $Ba_{n\cdot 5}Sr_{n\cdot 5}Co_{n\cdot 8}Fe_{n\cdot 2}O_{3-\delta}$, Fe-N-C catalysts, and benchmark oxides like RuO_2 and IrO_2 – have highlighted critical insights into rate-determining steps (RDS) and the influence of electronic and structural properties on catalytic performance.

For comparison, the catalytic performance of the single-phase systems such as $FeNb_2O_6$ and $MnNb_2O_6$ was also evaluated, including implicit solvation effects. In $FeNb_2O_6$ (Figure 7d), Fe sites exhibit a minimum overpotential of 1.22 V, driven by moderate binding energies of OER intermediates. In contrast, Nb sites exhibit a higher overpotential of 1.73 V due to stronger binding of O* intermediates. Similarly, in $MnTa_2O_6$ (Figure 7e), Mn sites demonstrate an overpotential of 1.35 V, reflecting their moderate catalytic activity. Distinctly, Ta sites again show stronger intermediate adsorption, leading to a higher overpotential of 1.78 V. These observations highlight the catalytic dominance of Fe and Mn as redox-active centers, with B sites playing a secondary role by stabilizing critical reaction intermediates. A similar trend is observed in $FeMn(NbTa)_2O_6$ and $MnNb_2O_6$. For the $FeMn(NbTa)_2O_6$ catalyst (Figure 7f), Fe and Mn sites demonstrate moderate overpotentials of 1.04 and 1.13 V, respectively, while Nb and Ta sites show higher overpotentials of 2.02 and 1.54 V, respectively, due to the strong stabilization of *OH and *OOH intermediates. Likewise, in $MnNb_2O_6$ (Figure 7g), Mn sites achieve a moderate overpotential of 1.26 V, whereas Nb sites exhibit a higher overpotential of 1.86 V. Importantly, while Fe and Mn sites exhibit lower overpotentials than Nb and Ta, adsorption preferences must also be considered. The O, OH, and OOH intermediates preferentially adsorb at Nb and Ta sites due to their higher adsorption energies. However, this strong adsorption can lead to slower reaction kinetics, as the release of intermediates or products becomes energetically demanding. In contrast, the moderate adsorption energies at Fe and Mn sites are sufficient to stabilize intermediates for further catalytic transformation, particularly favoring the formation of O*, which is critical for efficient OER catalysis. As a result, despite weaker initial adsorption, Fe and Mn sites promote more favorable reaction kinetics and lower overall overpotentials, making them the primary active centers in OER. Consistently, the rate-determining step (RDS) for $FeMn(NbTa)_2O_6$ (010) is identified as the third elementary reaction step, corresponding to the transition from O to OOH. This step is facilitated by the relatively weaker O binding energies on Fe and Mn sites, with ΔG_3 values of 1.64 eV for Fe and 1.13 eV for Mn, allowing efficient intermediate turnover. In contrast, Nb

and Ta sites exhibit stronger O binding, resulting in significantly higher ΔG_3 values of 2.03 eV for Nb and 1.67 eV for Ta. Notably, while Mn remains somewhat potential-limited by ΔG_3, it is to a lesser extent than Nb/Ta, and Fe exhibits a more even distribution of potential-limiting steps across the reaction.[67] This observation aligns with molecular theory, which suggests that the strength of the M-OH bond decreases with an increase in the *d*-electron count of the transition metal ion. Thus, Fe and Mn within AO_6 arrangements are associated with high redox metal reactivity, consistent with the proposed mechanism wherein the formation of the O-O bond involves the coupling of two OH intermediates.[68] Metal *d* orbitals of Nb and Ta can effectively interact with the antibonding orbitals of the OOH species.[68,69] These metal *d* orbitals may have appropriate energies and spatial distributions to form bonding interactions with the OOH* molecule. For instance, the empty *d* orbitals of the metal center can overlap with the antibonding orbitals of OOH*, stabilizing the adsorbed state. This interaction helps in reducing the energy required for the reaction to proceed by lowering the activation barrier. Additionally, the presence of metal sites can influence the electronic structure of the OOH* species upon adsorption. The interaction with the metal *d* orbitals alters the energy levels and distribution of electrons within the OOH* molecule.[41] This electronic restructuring of the OOH* species can further stabilize its adsorbed state on the metal surface, thereby facilitating specific redox reactions.[6,47] The stronger affinity and reduced energy barrier for BO_6 sites highlight their predominant role in *O adsorption energy.[14b,70] This is consistent with a general trend observed in previous literature, wherein transition metals of Group 5 with partially filled *d* orbitals are associated with greater redox reactivity.[5,70]

The efficiency of alkaline water reduction processes is significantly hindered, negatively impacting hydrogen production and reaction kinetics. As shown in Figure S55, Supporting Information, the evaluation of H_2O binding energies on $FeMn(NbTa)_2O_6$(010) catalysts reveal that H_2O adsorption is thermodynamically most favorable on Ta (E_{ads} = −1.88 eV), followed by Nb (E_{ads} = −1.78 eV), Mn (E_{ads} = −1.43 eV), and Fe (E_{ads} = −1.37 eV). This trend aligns with the electronegativity and electronic configurations of Nb and Ta, which likely lead to stronger interactions with water molecules due to their oxophilicity and ability to form covalent bonds with oxygen.[71] Mn shows an optimal energy barrier for water dissociation (E_{act} = 0.42 eV) compared to Fe (E_{act} = 0.51 eV), Ta (E_{act} = 0.66 eV), and Nb (E_{act} = 0.79 eV), indicating a greater efficiency for surface $H_2O \rightarrow$ *OH + H dissociation. In the subsequent phase of dissociation, E_{ads} for Fe (−1.63 eV), Mn (−1.77 eV), Ta (−2.35 eV), and Nb (−2.43 eV) are calculated for the binding of OH and H to underlying oxygen atoms (O-H). This suggests that B-sites have a higher propensity to adsorb H_2O than A-sites. This behavior is attributed to the presence of oxophilic metals in $FeMn(NbTa)_2O_6$ (010), which favor water splitting. We investigated the solvation effects on water adsorption and dissociation energetics, as well as the Gibbs free energies of hydrogen adsorption (ΔG_{H^*}). Figure 7i and Table S12, Supporting Information show that solvation stabilizes the water molecule by 0.32–0.43 eV at the different binding sites on $FeMn(TaNb)_2O_6$(010) surfaces. By stabilizing the products (H^+ and OH^-), we find that the inclusion of solvent reduced the activation barrier for water dissociation. The solvation energy for H* is predicted to be in the range of 0.07–0.19 eV at the different binding sites on $FeMn(TaNb)_2O_6$(010) surfaces, which is similar to the range predicted for hydrogen on Pt(111), 0.04–0.17 eV.[72] Furthermore, proton (H*) adsorption (Figure S56, Supporting Information) with A-sites acting as proton acceptors directs dissociated $2H^* + 2e^- \rightarrow H_2$ desorption steps, with the slightly greater closeness of their ΔG_{H^*} values to zero indicating optimum H adsorption on the electron-deficient Fe or Mn sites.[66b] For an active HER catalyst, the value of ΔG_{H^*} must be close to zero, indicating that the free energy of adsorbed H is close to that of the reactant or product.[73] The calculated Gibbs free energy of hydrogen adsorption at different sites on $FeMn(NbTa)_2O_6$ (010) catalysts with and without solvation effects is shown in Figure 7k,l. When adsorbed on oxygen sites coordinating with different cations: $O_{\text{-Fe}}$ (ΔG_{H^*} = −0.21 eV), $O_{\text{-Mn}}$ (ΔG_{H^*} = −0.31 eV), $O_{\text{-Nb}}$ (ΔG_{H^*} = −0.59 eV), and $O_{\text{-Ta}}$ (ΔG_{H^*} = −0.60 eV) values suggest favorable hydrogen adsorption at the oxygen surface sites. In contrast, a positive ΔG_{H^*} is calculated at Fe (ΔG_{H^*} = 0.23 eV) and Mn (ΔG_{H^*} = 0.37 eV) sites on $FeMn(NbTa)_2O_6$ (010) surfaces, indicating unfavorable and weak hydrogen adsorption. The Nb (ΔG_{H^*} = −0.68 eV) and Ta (ΔG_{H^*} = −0.74 eV) sites on the other hand show negative adsorption energies, suggesting that Nb 4*d* and Ta 5*d* likely have valence shell configurations (outermost electrons such as 5*s* and 6*s*, respectively) facilitating strong interactions with hydrogen.[74] Figure 7k,l shows a volcano-type HER mechanism based on the Sabatier principle, assuming the Volmer step is rate-determining and that H* adsorption obeys a Langmuir isotherm. The first assumption is appropriate given Fe and Mn weakly adsorb H*, as the RDS would be either the Tafel or Heyrovsky step if the maximum exchange current density was near $\Delta G^0_{Hads} = 0$. When $\Delta G_{H^*} > 0$, the adsorption of H* is weak, resulting in an exponential increase of exchange current density (j_0) as ΔG_{H^*} decreases.[75] Conversely, when $\Delta G_{H^*} < 0$, the adsorption of H* is strong. This occurs on Ta and Nb sites and proportionally on oxygen neighboring metal sites in $FeMn(NbTa)_2O_6$, causing exchange current density (j_0) to exponentially decrease as ΔG_{H^*} decreases.

3. Conclusion

In this study, we employed a conventional sol-gel crystallization method, followed by hydrothermal treatment of colloidal solution, to synthesize columbite-type AB_2O_6 phases, including $FeNb_2O_6$, $FeTa_2O_6$, $MnNb_2O_6$, $MnTa_2O_6$, and $FeMn(NbTa)_2O_6$. The initially amorphous and poorly crystallized particles were then annealed at 1200 °C in an H_2/Ar atmosphere to enhance crystallinity and introduce interstitial lattice defects. These high-quality, orthorhombically structured phases pave the way for developing multicomponent columbite-based catalysts with enhanced electrocatalytic performance and stability, showing great promise for applications in alkaline electrolyzers. This synergy – combined with high activity, stability, and site density – enabled $FeMn(NbTa)_2O_6$ to achieve a lower potential at 100 mA cm^{-2} for OER/HER initiation compared to its counterparts $FeNb_2O_6$, $FeTa_2O_6$, $MnNb_2O_6$, and $MnTa_2O_6$, which required slightly higher potentials. Furthermore, when applied in an anion exchange membrane water electrolyzer (AEMWE) assembly, $FeMn(NbTa)_2O_6$ displayed competitive performance, achieving a cell voltage of 1.81 V at 0.7 A cm^{-2}, closely matching the

performance of the benchmark 40% Pt/C-RuO_2 catalyst. Durability tests further highlighted $FeMn(NbTa)_2O_6$'s robustness, as it maintained a stable cell voltage of approximately 1.85 V over 200 h of continuous operation.

Density functional theory (DFT) simulations further elucidate the pivotal role of Nb and Ta at the B-sites. These high-valence centers promote favorable d-band alignment, strengthening interactions between metal d-orbitals and oxygen p-orbitals. This alignment lowers activation barriers for reaction intermediates, facilitates electronic delocalization, and minimizes charge accumulation, collectively enhancing conductivity and catalytic activity. Notably, while Nb and Ta exhibit stronger adsorption for OER intermediates (O*, OH*, OOH*), this may lead to higher energy barriers for product release. In contrast, Fe and Mn demonstrate moderate adsorption energies that strike a balance between stable intermediate binding and favorable desorption critical for efficient O_2 evolution.

Complementing this, Fe and Mn at the A-sites exhibit strong redox reactivity and high affinity for OH* and O* intermediates, contributing to efficient electron transfer. The low t_2g and e_9 valence peaks near the conduction band edge on Nb and Ta further support rapid electron transfer and reduce OOH* formation energy. This dual-site synergy balances strong initial adsorption of intermediates with favorable desorption of OOH*, significantly lowering the activation energy for key steps in both OER and HER. Furthermore, solvation effects were incorporated using the implicit electrolyte model (VASPsol) to reflect more realistic operating conditions. The results show that solvation significantly stabilizes the O*, OH*, and OOH* intermediates but especially O*, thereby reducing the activation energy for water dissociation.

In situ X-ray absorption spectroscopy (XAS) reveals dynamic coordination changes in Fe, Mn, Nb, and Ta under operating conditions. The observed structural flexibility and coordination dynamics corroborate the theoretical predictions, confirming the strong interactions between surface sites and adsorbed intermediates. This synergistic interplay of A-site and B-site metals in the columbite framework enables a robust charge transfer pathway, resulting in superior electrocatalytic performance, reduced overpotentials, and enhanced durability in alkaline water electrolyzer.

4. Experimental Section

Reagents: Ammonium niobate (V) oxalate hydrate ($C_4H_4NNbO_9{\cdot}xH_2O$, 99.99% trace metal basis), tantalum (V) chloride ($TaCl_5$, 99.8% trace metal basis), absolute ethanol (C_2H_5OH, 99.9%), potassium hydroxide (KOH), and sodium hydroxide (NaOH) were purchased from Sigma Aldrich, Merck Korea. Iron (II) sulfate heptahydrate ($FeSO_4.7H_2O$, 98.0% pure) and hydrogen hydrofluoric acid (HF, 49%) were purchased from Pure Co. Ltd (Korea). Manganese (II) sulfate monohydrate ($MnSO_4.H_2O$, 99%) was purchased from Acros Organics. All the chemicals and reagents are of analytical grade and were used without further purification. The reagents were freshly prepared in ultrapure water and purified using a Millipore-Q system.

Synthesis of Active Materials: The AB_2O_6-columbite active material was synthesized using three steps in a simple procedure, as illustrated in Figure 1a. The facile hydrothermal procedure was selected for the preparation of $FeMn(TaNb)_2O_6$ precursors. Typically, 2.0 mL of 0.1 M $MnSO_4.H_2O$, 2.0 mL of 0.1 M $FeSO_4.7H_2O$, and 2 mL of 0.2 M $C_4H_4NNbO_9{\cdot}xH_2O$ prepared in ultrapure distilled water were mixed with 2 mL of 0.2 $TaCl_5$ prepared via 1.0 M HF in a 20 mL glass vial. This mixture was sonicated for 1 h in a water bath, followed by vigorous stirring for 30 min. Subsequently, the mixture was treated with 2.0 M NaOH drop-by-drop until its pH reached 11, and the obtained colloidal solution was stirred for another half an hour. Afterward, the colloidal solution was transferred into a 100 mL Teflon-lined tube and subjected to hydrothermal treatment at 180 °C for 24 h. After the hydrothermal device naturally cooled down to room temperature, a dirty brownish solid product was obtained. Thus, the obtained precipitate was washed several times with deionized water and ethanol, in order to eliminate impurities. In the second step, the washed precipitate was kept at −80 °C for 12 h and then transferred to a freeze dryer (ILShin BioBase Co. Ltd., Republic of Korea) for lyophilization. Finally, the sample was calcined at 1200 °C for 8 h (tube furnace, DAIHAN Scientific), at a heating rate of 5 °C min^{-1} under H_2/Ar atmosphere. All the samples were sieved at a diameter of 150 µm, washed to neutral pH with distilled water, and dried at 105 °C for 24 h in an oven dryer before application. The obtained $FeMn(NbTa)_2O_6$ was compared with $FeNb_2O_6$, $MnTa_2O_6$, $MnNb_2O_6$, and $FeTa_2O_6$ prepared under the same experimental conditions, namely by taking their respective precursor solutions in the first step.

Materials Characterizations: To elucidate the presence of the different peaks of all materials, ex situ High-Resolution Powder Diffraction (HRPD) patterns of $FeNb_2O_6$ (FNO), $FeTa_2O_6$ (FTO), $MnNb_2O_6$ (MNO), $MnTa_2O_6$ (MTO), $FeMn(TaNb)_2O_6$-110 (TNO-110), and $FeMn(TaNb)_2O_6$-1200 (TNO-1200) were resolved via beamline 9B of the Pohang Light Source (PLS) at the Pohang Accelerator Laboratory. All measurements were collected at an average incident beam count of 10 330.5 (max: 10 752.0, min: 9961.0, start: 9.00, step: 0.0050, stop: 29.50). For this characterization, a multipurpose X-ray Diffraction (XRD) analyzer (X'pert Pro, PANalytical, the Netherlands) was also used with high-intensity monochromatic Cu-Kα radiation as an incident beam (λ = 1.54 Å) at the Center for University-Wide Research Facilities (CURF) of Jeonbuk National University. To evaluate specific surface areas and pore size distributions, N_2-sorption analyses were conducted on an ASAP 2020 Plus system (Micromeritics Instrument Corp., USA) at Korea Basic Science Institute (KBSI) Jeonju Center. Barrett–Joyner–Halenda (BJH) analysis based on N_2-sorption was used for pore size distributions. Surface morphology was observed by field emission scanning electron microscopic (FE-SEM) images, and the elemental compositions of materials were tested by Energy Dispersive X-ray Spectroscopy (EDS) equipped in the CURF(Supra 40 V P instrument Zeiss Co., Germany). The phase images and surface roughness of the composite membranes were analyzed using the TM-AFM Bruker Multimode-8 atomic force microscope (AFM) in tapping mode at the CURF. The Raman spectrum of each manufactured electrocatalyst was measured using elevated 3D mapping scanning Raman spectroscopy with a NANO PHOTON (RAMAN Touch) outfitted with a 532 nm He-Ne laser at the CURF. The microstructure characteristics were examined by using Cs_corrected-Field transmission electron microscopy (STEM) and High-Resolution Scanning Transmission Electron Microscopy (HR-STEM) after having the samples ultrasonically dispersed in ethanol and drop cast onto a 300 mesh Cu coated with Lacey F/C (Model: JEM-2200FS instrument JEOL Co., USA). Scanning TEM (STEM) and complementary EDS were also employed for elemental mapping.

Chemical compositions were obtained by hybrid x-ray photoelectron spectrometry (XPS) with ultra-violet source (UPS) analysis, using as-prepared electrodes washed thoroughly with water and dried at 60 °C overnight under vacuum. XPS spectra were obtained by Nexsa XPS system, Thermo Fisher Scientific using Al Kα radiation at the KBSI Jeonju Center.

Ex and In Situ X-ray Absorption Spectroscopy: To investigate the local electronic structure and local coordination of metals centers, hard X-ray absorption spectroscopy (XAS) was conducted at the Fe K-edge (≈7.1 keV), Mn K-edge (6.5 KeV), Nb K-edge (≈19 keV), and Ta L_3-edge (≈9.8 keV) in fluorescence yield mode at 8C beamline in Pohang Light Source (PLS). The in situ XAS measurements were conducted at different applied currents, namely the open circuit potential (OCP), −10, 10, and 20 mA in fluorescence yield mode at X-ray absorption fine structure 10C beamline in the PLS. The Fourier transformation (FT) of the extended X-ray absorption fine structure (EXAFS) was processed using ATHENA

within a range of electron momentum (k) of 3–13 $Å^{-1}$ after scaling by k^2.

Electrochemical Characterization—Electrochemical Oxygen and Hydrogen Evolution Reaction Measurements: The electrochemical study of all materials was performed using a CH electrochemical workstation (CH660-CH instrument) in a standard three-electrode configuration using a material piece, an Ag/AgCl electrode, and a graphite rod electrode serving as a working electrode, a reference electrode, and a counter electrode, respectively. The cyclic voltammetry (CV) and linear sweep voltammetry (LSV) measurements of AB_2O_6 in O_2-saturated 1 M KOH were collected using a three-electrode setup at scan rates of 2 and 5 mV s^{-1}, with conversion to the reversible hydrogen electrode (RHE) and using Ag/AgCl.

$$E_{RHE} = E_{\frac{Ag}{AgCl}} + 0.59 \times pH + E^{o}_{\frac{Ag}{AgCl}} \quad (6)$$

Electrochemical active surface area (ECSA): The CV was scanned at various scan rates (no-Faradaic zone) in all three electrolytes to measure the C_{dl} of the materials. ECSA were converted from CV at different scan rates within the no-Faradaic zone via the equation: $i_c = \nu C_{dl}$ (i_c = charging current, v = scan rate, C_{dl} = double layer capacitance). Then, ECSA = $\frac{C_{dl}}{C_s}$, with a carbon cloth geometric area (GSA) equal to 0.98 cm^2 and Roughness factor (RF) = $\frac{ECSA}{GSA}$. Electrochemical impedance spectroscopy (EIS) was conducted at the open circuit potential in the frequency range from 0.01 HZ to 100 kHz. Stability tests were conducted by chronopotentiometry at 0.01, 0.2 and 0.4 A cm^{-2} in 20 and 30% KOH solution at 60 °C, using $FeMn(TaNb)_2O_6$ spray coated on the Nickel foam electrode.

TOF (turnover frequency) is defined as the number of catalytic events (in this case, 6 electrons transferred) per unit time per unit active site. First, we calculated the number of active sites on the electrode surface. Assuming a monolayer coverage of $FeMn(NbTa)_2O_6$ on the electrode surface, we estimate the surface area of the electrode covered by the catalyst: $A\,(cm^2) = \frac{m(g)}{Density\ in\ \frac{g}{cm3}} * \frac{1}{H(cm)}$; assuming a density of $FeMn(NbTa)_2O_6$ of 5.68 g cm^{-3}, and a thickness of a monolayer as 1 nm (10^{-7} cm), we get: $A = 8.8\ cm^2$. Thus, the number of active sites on the electrode surface can be calculated as:

$$N = \frac{n*A}{Aw} \quad (7)$$

where $N = number\ of\ active\ sites$, n = Avogadro's number = 6.022 x 10^{23}, A = surface area, and AW = atomic weight of $FeMn(NbTa)_2O_6$ = 452.23 g mol^{-1}. Thus:

$$N = \frac{6.022\ 10^{23} * 8.8}{452.23} = 1.18 \times 10^{22} \quad (8)$$

Now, we can calculate the TOF at a J of 10 mA cm^{-2} as: $TOF = \frac{-J(Curent\ density)}{n*F*N}$, where J is the current, n is the number of electrons transferred (in this case, 6), F is the Faraday constant (96 485 C mol^{-1}), and the negative sign accounts for the fact that we are considering the OER. At 10 mA cm^{-2}, the current density is 0.1 A cm^{-2}. Therefore: $TOF = \frac{-0.01\ \frac{A}{cm2}}{6*96485^{c}_{mo}*\ 1.18\ 10^{22}} = 1.45 \times 10^{-10} S^{-1}$

Mass activity conversion:

$Mass = \frac{Mass\ of\ TNO}{AW\ \frac{g}{mol}} = \frac{16.8\ mg}{214.33\ \frac{g}{mol} * 1000\ \frac{mg}{gl}} = 7.82x10^{-5}\ mole$. Given a current (I) at the given current density (j = 50 mA cm^{-2}) and an electrode area (0.5 cm^2), mass activity is $a = \frac{I}{Mass} = \frac{25\ mA}{7.82\ 10^{-5}\ mole} = 3.20 \times 10^{-8}\ \frac{mA}{g}$. Therefore, the mass activity of the $FeMn(TaNb)_2O_6$ electrode is equal to 3.20×10^8 mA g^{-1}.

Electrochemical Characterization—Anion Exchange Membrane Water Electrolyzer Single Cell Test: A commercial 2-cell stack (3-Layer MEA) with a Sustainion *37–50 Grade RT membrane and 5 cm^2 parallel flow fields was used, with any TiO_2 cleaned from the Ti cathode's Porous Transport Layer (PTL) before assembly. The anode and cathode were assembled using 40% Pt/C-RuO_2 compared with $FeMn(TaNb)_2O_6$-$FeMn(TaNb)_2O_6$, $FeNb_2O_6$-$MnNb_2O_6$, Fe_2O_3-MnO, Nb_2O_5, and Ta_2O_5. Prior to use, the Sustainion *37–50 Grade RT membrane (measuring 6 cm × 6 cm) was soaked in 1 M KOH for over 24 h, and the active working electrode area was set to 5 cm × 5 cm in the single–cell configuration. The cathode and anode catalyst ink was prepared by dispersing 60 mg in 1 mL solvent solution (LIQUion-H_2O water based 1100 EW at 10% weight) with 20 µl Nafion solution (0.5% wt.). The ink was spray-coated onto a GDL substrate with a spray gun connected via N_2 carrier gas and heated on a manual hot plate at 140 °C (4000 psi, hydraulic press). A self-priming pump with a flow rate of 30 mL min^{-1} was used to recirculate alkaline electrolyte (30% KOH, UN 1814, reagents DUKSAN) between the anode side and an electrolyte reservoir. The electrolyzer was heated, and the temperature (60 °C) was precisely controlled with an automatic temperature control device. Once the temperature of the cell was stabilized, its performance was analyzed. All electrochemical tests in this study were conducted on single cells. The polarization curves (LSV, LSC and stability) of the AEM single cell were evaluated by a CNL Electrolyzer system (Korea) at the range 1.0–3.0 V and a scan rate of 5 mV s^{-1}.

Computational Details: The density functional theory (DFT) calculations were performed within VASP (Vienna ab-initio simulation package).[76] The electron-ion interactions were described using the projector augmented wave (PAW) pseudopotentials method.[77] The Perdew–Burke–Ernzerhof (PBE) exchange-correlation functional with Hubbard correction (DFT+U) was used for the on-site Coulomb Repulsion.[78] In the present work, an effective U value of 5.0 for Fe, Mn, Ta, and Nb was found to provide an accurate description of the structural parameters and the electronic properties of $FeNb_2O_6$, $FeTa_2O_6$, $MnNb_2O_6$, $MnTa_2O_6$, and $FeMn(TaNb)_2O_6$. All calculations were spinpolarized. An energy cut-off of 500 eV was used to expand the electronic wave functions, which was sufficient to converge the total energy and the Hellman–Feynman forces to within 10^{-6} eV and 0.001 eV $Å^{-1}$, respectively. Van der Waals (vdW) dispersion forces were accounted for using the Grimme DFT-D3 scheme. The $FeMn(TaNb)_2O_6$ (010) surface, consisting of a total of 144 atoms (8 Fe, 8 Mn, 16 Nb, 16 Ta, and 96 O) distributed over eight atomic layers, was used to characterize the OER and HER processes. The topmost five layers of the slab were allowed to relax without constraint, while the bottom three were kept fixed at their relaxed bulk positions to simulate the bulk phase of the crystal. Monkhorst-Pack k-point meshes of 3 × 9 × 9 and 3 × 3 × 1 were used to sample the Brillouin zones of the bulk materials and the (010) surfaces, respectively. A 2 × 2 supercell of the most stable (010) surface was used to characterize the HER and OER processes, predicting the structures and energetics of adsorbates. This is large enough to minimize lateral interactions in periodic cells. In each simulation cell, a vacuum size of 15 Å was used in the c-direction to prevent interaction between periodic slabs. The OER occurred following the 4e-mechanism proposed by Norskov for water oxidation.[66]

$$* + H_2O \rightarrow HO* + \left(H^+ + e^-\right) \Delta GI \quad (9)$$

$$HO* \rightarrow O* + \left(H^+ + e^-\right) \Delta GII \quad (10)$$

$$O* + H_2O \rightarrow HOO* + \left(H^+ + e^-\right) \Delta GIII \quad (11)$$

$$HOO* \rightarrow * + O_2 + \left(H^+ + e^-\right) \Delta GIV \quad (12)$$

Here, * denotes the active sites on the surface and *O*, HO*, and HOO** denote the adsorbed oxygenated species. ΔG_I, ΔG_{II}, ΔG_{III}, *and* ΔG_{IV} represent the reaction Gibbs free energies. The overpotential (η) of the OER for each of the catalysts has been evaluated using the following equation:$\eta = \frac{Max(\Delta GI,\ \Delta GII,\ \Delta GIII,\ \Delta GIV)}{e} - 1.23\ V$, where $\Delta G_I = \Delta G_{OH*}$; $\Delta G_{II} = \Delta G_{O*} - \Delta G_{OH*}$; $\Delta G_{III} = \Delta G_{OOH*} - \Delta G_{O*}$; and $\Delta G_{IV} = 4.92 -$

ΔG_{OOH*}. The adsorption energies of O (ΔE_{O*}), OH (ΔE_{OH*}), and OOH (ΔE_{OOH*}) on Fe, Mn, Nb, and Ta were determined as:

$$\Delta E_{O*} = E_{O*} - E_{*} - [E_{H2O} - E_{H2}] \quad (13)$$

$$\Delta E_{OH*} = E_{OH*} - E_{*} - [E_{H2O} - \frac{1}{2}E_{H2}] \quad (14)$$

$$\Delta E_{OOH*} = E_{OOH*} - E_{*} - [2E_{H2O} - \frac{3}{2}E_{H2}] \quad (15)$$

Here, E_{*} *and* $E_{O*}/E_{OH*}/E_{OOH*}$ are the respective DFT energies of the clean $FeNb_2O_6$, $FeTa_2O_6$, $MnNb_2O_6$, $MnTa_2O_6$, and $FeMn(TaNb)_2O_6$ (010) surfaces and matching surfaces with corresponding adsorbates, while E_{H2O} and E_{H2} are the DFT energies of H_2O and H_2 molecules. Using these adsorbate energetics, the Gibbs free energy (ΔG) is calculated using the relation:

$$\Delta G = \Delta E + \Delta E_{ZPE} - T\Delta S + \Delta G_U - \Delta G_{pH} \quad (16)$$

where ΔE is the reaction energy obtained from DFT adsorbate calculations, ΔE_{ZPE} is the difference in zero point energy between adsorbed and gas phases, and ΔS is the entropy associated with the adsorption reaction scaled by temperature (T).[79] The Gibbs free energy electrochemical contribution is resolved via: $\Delta G_U = -neU$, where n is the number of electrons transferred, e is the elementary charge of an electron, and U is the electrode potential. The solvation effect is included by the implicit electrolyte model implemented in VASPsol, with a Debye length of 3.0 Å that corresponds to a 1 M ionic strength and a dielectric constant of 78.4 for the aqueous solution.[63] The solvation energy is defined by ΔE_{sol} (eV) = $E_{solv} - E_{gas}$, where E_{solv} and E_{gas} are the total energy of the system with and without solvation included, respectively. Single-point calculations were carried out to include the solvent effect. By this definition, a more negative solvation energy implies higher stabilization of the species due to solvation.

Supporting Information

Supporting Information is available from the Wiley Online Library or from the author.

Acknowledgements

This work was funded by The Regional Leading Research Center Program (2019R1A5A8080326) through the National Research Foundation funded by the Ministry of Science and ICT of the Republic of Korea and supported by grants from the Basic Science Research Program through the National Research Foundation of Korea (NRF) by Ministry of Education, Science and Technology (Project no. RS-2024-00335915). N.K. and N.Y.D. acknowledge U.S. Department of Energy, Office of Science, Basic Energy Sciences, Early Career Program, under Award No. DOE DE-SC0025350. Computations for this research were performed on the Pennsylvania State University's Institute for Computational and Data Sciences' Roar. P.M.B. is thankful for the assistance received from Dr. Che-Ryong Lim and Prof. Yeoung-Sang Yun of the Division of Semiconductor and Chemical Engineering at Jeonbuk National University in the Republic of Korea, to allow the authors to conduct some parts of the experiments in his laboratory. We gratefully acknowledge the Helmholtz Association's Initiative and Networking Fund (Helmholtz Young Investigator Group VH-NG-1719) for the funding. We are thankful to the Center for University-wide Research Facilities (CURF), JeonbukNational University, Jeonju, South Korea for XRD, ICP, XPS, FTIR, AFM, Raman, and FE-SEM/EDS facilities. We are also thankful to the Korea Basic Science Institute (KBSI), Jeonju, South Korea for N_2 corrected-Field transmission electron microscopy (STEM) analysis.

Conflict of Interest

The authors declare no conflict of interest.

Author Contributions

P.M.B. contributed to the research design, materials synthesis, data analysis, and the manuscript writing and redaction. D.S., E.M.H. and K.K. carried out the synthesis experiments and manuscript redaction. M.B.P., Y.D. assisted on the electrochemical cell experiments. E.S.J., A.Y.M., B.H., D.Y.C. conducted the X-ray adsorption data analysis. N.K., N.Y.D. performed the theoretical calculations, and manuscript editing. M.B.A., M.P.B., M.T.C., G.H.G., J.W.H. assisted on the DFT calculations, data visualization, and manuscript redaction. C.H.P. directed, supervised the planning, and secured the funding of this research. All authors discussed the results and contributed to the manuscript redaction.

Data Availability Statement

The data that support the findings of this study are available in the supplementary material of this article.

Keywords

alkaline water electrolyzer, anion exchange membrane, charge transfer, columbite-type AB_2O_6 , metal redox reactivity, in situ XAS findings

Received: September 28, 2024
Revised: March 27, 2025
Published online: April 15, 2025

[1] Z. Wan, Y. Zhang, Q. Ren, X. Li, H. Yu, W. Zhou, X. Ma, C. Xuan, *J. Colloid Interface Sci.* **2024**, *653*, 795.
[2] Z. He, Y. He, Y. Qiu, Q. Zhao, Z. Wang, X. Kang, L. Yu, L. Wu, Y. Jiang, *Appl. Catal., B* **2024**, *342*, 123386.
[3] M.-A. Ha, S. M. Alia, A. G. Norman, E. M. Miller, *ACS Catal.* **2024**, *14*, 17347.
[4] Y. Zhou, S. Sun, C. Wei, Y. Sun, P. Xi, Z. Feng, Z. J. Xu, *Adv. Mater.* **2019**, *31*, 1902509.
[5] X. Wang, S. Xi, P. Huang, Y. Du, H. Zhong, Q. Wang, A. Borgna, Y.-W. Zhang, Z. Wang, H. Wang, Z. G. Yu, W. S. V. Lee, J. Xue, *Nature* **2022**, *611*, 702.
[6] B. Zhang, L. Wang, Z. Cao, S. M. Kozlov, F. P. García de Arquer, C. T. Dinh, J. Li, Z. Wang, X. Zheng, L. Zhang, Y. Wen, O. Voznyy, R. Comin, P. De Luna, T. Regier, W. Bi, E. E. Alp, C.-W. Pao, L. Zheng, Y. Hu, Y. Ji, Y. Li, Y. Zhang, L. Cavallo, H. Peng, E. H. Sargent, *Nat. Catal.* **2020**, *3*, 985.
[7] M. Novák, Z. k. Johan, R. Skoda, P. Černý, V. R. Srein, F. E. Veselovský, *Eur. J. Mineral.* **2008**, *20*, 487.
[8] a) E. E. Nikishina, D. V. Drobot, E. N. Lebedeva, *Russian Journal of Non-Ferrous Metals* **2013**, *54*, 446; b) A. Rafieerad, A. Amiri, G. L. Sequiera, W. Yan, Y. Chen, A. A. Polycarpou, S. Dhingra, *Adv. Funct. Mater.* **2021**, *31*, 2100015.
[9] P. M. Bacirhonde, N. Y. Dzade, C. Chalony, J. Park, E.-S. Jeong, E. O. Afranie, S. Lee, C. S. Kim, D.-H. Kim, C. H. Park, *ACS Appl. Mater. Interfaces* **2022**, *14*, 15090.
[10] P. M. Bacirhonde, A. Y. Mohamed, B. Han, D.-Y. Cho, S. Devendra, J.-W. Choi, C.-R. Lim, E. O. Afranie, K.-H. Baik, K. Kang, S. Lee, E.-S. Jeong, N. Komalla, N. Y. Dzade, C. H. Park, C. S. Kim, *Adv. Energy Mater.* **2023**, *13*, 2300174.

[11] P. M. Bacirhonde, A. Y. Mohamed, B. Han, D. Y. Cho, S. Devendra, J. W. Choi, C. R. Lim, E. O. Afranie, K. H. Baik, K. J. A. E. M. Kang, *Adv. Energy Mater.* **2023**, *13*, 2300174.
[12] Y.-R. Zheng, J. Vernieres, Z. Wang, K. Zhang, D. Hochfilzer, K. Krempl, T.-W. Liao, F. Presel, T. Altantzis, J. J. N. E. Fatermans, *Nat. Energy* **2022**, *7*, 55.
[13] W. Wang, X. Wang, J. Shan, L. Yue, Z. Shao, L. Chen, D. Lu, Y. J. E. Li, *Energy Environ. Sci.* **2023**, *16*, 2669.
[14] a) J. C. Ruiz-Cornejo, D. Sebastián, M. V. Martínez-Huerta, M. J. Lázaro, *Electrochim. Acta* **2019**, *317*, 261; b) Y.-R. Zheng, J. Vernieres, Z. Wang, K. Zhang, D. Hochfilzer, K. Krempl, T.-W. Liao, F. Presel, T. Altantzis, J. Fatermans, S. B. Scott, N. M. Secher, C. Moon, P. Liu, S. Bals, S. Van Aert, A. Cao, M. Anand, J. K. Nørskov, J. Kibsgaard, I. Chorkendorff, *Nat. Energy* **2022**, *7*, 55.
[15] S. Sun, Y. Zhang, X. Shi, W. Sun, C. Felser, W. Li, G. Li, *Adv. Mater.* **2024**, *36*, 2312524.
[16] W. Wang, X. Wang, J. Shan, L. Yue, Z. Shao, L. Chen, D. Lu, Y. Li, *Energy Environ. Sci.* **2023**, *16*, 2669.
[17] a) J. Xu, H. Jin, T. Lu, J. Li, Y. Liu, K. Davey, Y. Zheng, S.-Z. Qiao, *Sci. Adv.* **2023**, *9*, 1718; b) J. C. Ruiz-Cornejo, D. Sebastián, M. Martínez-Huerta, M. Lázaro, *Electrochim. Acta* **2019**, *317*, 261.
[18] Y.-R. Zheng, J. Vernieres, Z. Wang, K. Zhang, D. Hochfilzer, K. Krempl, T.-W. Liao, F. Presel, T. Altantzis, J. Fatermans, *Nat. Energy* **2022**, *7*, 55.
[19] E. Trenkenschuh, W. Friess, *Eur. J. Pharm. Biopharm.* **2021**, *165*, 345.
[20] M. Kim, J. Park, H. Ju, J. Y. Kim, H.-S. Cho, C.-H. Kim, B.-H. Kim, S. W. J. E. Lee, *Energy Environ. Sci.* **2021**, *14*, 3053.
[21] M. Gich, C. Frontera, A. Roig, E. Taboada, E. Molins, H. Rechenberg, J. Ardisson, W. Macedo, C. Ritter, V. Hardy, *Chem. Mater.* **2006**, *18*, 3889.
[22] M. Radler, J. Cohen, G. Sykora, T. Mason, D. Ellis, J. Faber Jr, *J. Phys. Chem. Solids* **1992**, *53*, 141.
[23] N. V. Tarakina, A. P. Tyutyunnik, V. G. Zubkov, T. V. D'Yachkova, Y. G. Zainulin, H. Hannerz, G. Svensson, *Solid State Sci.* **2003**, *5*, 983.
[24] V. P. Filonenko, I. P. Zibrov, *Inorg. Mater.* **2001**, *37*, 953.
[25] a) J. Bak, T. G. Yun, J.-S. An, H. B. Bae, S.-Y. Chung, *Energy Environ. Sci.* **2022**, *15*, 610; b) J. Landon, E. Demeter, N. İnoğlu, C. Keturakis, I. E. Wachs, R. Vasić, A. I. Frenkel, J. R. Kitchin, *ACS Catal.* **2012**, *2*, 1793.
[26] M. Risch, K. A. Stoerzinger, B. Han, T. Z. Regier, D. Peak, S. Y. Sayed, C. Wei, Z. Xu, Y. Shao-Horn, *J. Phys. Chem. C* **2017**, *121*, 17682.
[27] P. Plate, C. Höhn, U. Bloeck, P. Bogdanoff, S. Fiechter, F. F. Abdi, R. van de Krol, A. C. Bronneberg, *ACS Appl. Mater. Interfaces* **2021**, *13*, 2428.
[28] Z. L. Zhao, Q. Wang, X. Huang, Q. Feng, S. Gu, Z. Zhang, H. Xu, L. Zeng, M. Gu, H. Li, *Energy Environ. Sci.* **2020**, *13*, 5143.
[29] J. He, G. Fu, J. Zhang, P. Xu, J. Sun, *Small* **2022**, *18*, 2203365.
[30] a) K. S. Exner, H. Over, *ACS Catal.* **2019**, *9*, 6755; b) A. Damjanovic, A. Dey, J. O. M. Bockris, *Electrochim. Acta* **1966**, *11*, 791.
[31] F. P. Lohmann-Richters, B. Abel, Á. Varga, *J. Mater. Chem. A* **2018**, *6*, 2700.
[32] S. Zhang, Y. Wang, S. Li, Z. Wang, H. Chen, L. Yi, X. Chen, Q. Yang, W. Xu, A. Wang, Z. Lu, *Nat. Commun.* **2023**, *14*, 4822.
[33] I. Roger, M. A. Shipman, M. D. Symes, *Nat. Rev. Chem.* **2017**, *1*, 0003.
[34] M. Lu, Y. Zheng, Y. Hu, B. Huang, D. Ji, M. Sun, J. Li, Y. Peng, R. Si, P. Xi, C.-H. Yan, *Sci. Adv.* **2022**, *8*, abq3563.
[35] E. Fabbri, M. Nachtegaal, T. Binninger, X. Cheng, B.-J. Kim, J. Durst, F. Bozza, T. Graule, R. Schäublin, L. Wiles, M. Pertoso, N. Danilovic, K. E. Ayers, T. J. Schmidt, *Nat. Mater.* **2017**, *16*, 925.
[36] a) R. Subbaraman, D. Tripkovic, K.-C. Chang, D. Strmcnik, A. P. Paulikas, P. Hirunsit, M. Chan, J. Greeley, V. Stamenkovic, N. M. Markovic, *Nat. Mater.* **2012**, *11*, 550; b) C. Roy, B. Sebok, S. B. Scott, E. M. Fiordaliso, J. E. Sørensen, A. Bodin, D. B. Trimarco, C. D. Damsgaard, P. C. K. Vesborg, O. Hansen, I. E. L. Stephens, J. Kibsgaard, I. Chorkendorff, *Nat. Catal.* **2018**, *1*, 820.
[37] J. D. Benck, T. R. Hellstern, J. Kibsgaard, P. Chakthranont, T. F. Jaramillo, *ACS Catal.* **2014**, *4*, 3957.
[38] Y. Jiao, Y. Zheng, M. Jaroniec, S. Z. Qiao, *Chem. Soc. Rev.* **2015**, *44*, 2060.
[39] J. Guo, J. Wang, Z. Wu, W. Lei, J. Zhu, K. Xia, D. Wang, *J. Mater. Chem. A* **2017**, *5*, 4879.
[40] X. Wang, Q. Zhang, C. Zhao, H. Li, B. Zhang, G. Zeng, Y. Tang, Z. Huang, I. Hwang, H. Zhang, S. Zhou, Y. Qiu, Y. Xiao, J. Cabana, C.-J. Sun, K. Amine, Y. Sun, Q. Wang, G.-L. Xu, L. Gu, Y. Qiao, S.-G. Sun, *Nat. Energy* **2024**, *9*, 184.
[41] Z. W. Seh, J. Kibsgaard, C. F. Dickens, I. Chorkendorff, J. K. Nørskov, T. F. Jaramillo, *Science* **2017**, *355*, aad4998.
[42] B. Guo, X. Yu, X.-G. Sun, M. Chi, Z.-A. Qiao, J. Liu, Y.-S. Hu, X.-Q. Yang, J. B. Goodenough, S. Dai, *Energy Environ. Sci.* **2014**, *7*, 2220.
[43] a) M.-R. Li, P. W. Stephens, M. Retuerto, T. Sarkar, C. P. Grams, J. Hemberger, M. C. Croft, D. Walker, M. Greenblatt; b) M.-R. Li, P. W. Stephens, M. Retuerto, T. Sarkar, C. P. Grams, J. Hemberger, M. C. Croft, D. Walker, M. Greenblatt, *J. Am. Chem. Soc.* **2014**, *136*, 8508.
[44] K. McColl, R. A. House, G. J. Rees, A. G. Squires, S. W. Coles, P. G. Bruce, B. J. Morgan, M. S. Islam, *Nat. Commun.* **2022**, *13*, 5275.
[45] M. Sathiya, G. Rousse, K. Ramesha, C. P. Laisa, H. Vezin, M. T. Sougrati, M. L. Doublet, D. Foix, D. Gonbeau, W. Walker, A. S. Prakash, M. Ben Hassine, L. Dupont, J. M. Tarascon, *Nat. Mater.* **2013**, *12*, 827.
[46] D. Liu, X. Li, S. Chen, H. Yan, C. Wang, C. Wu, Y. A. Haleem, S. Duan, J. Lu, B. Ge, P. M. Ajayan, Y. Luo, J. Jiang, L. Song, *Nat. Energy* **2019**, *4*, 512.
[47] A. Grimaud, W. T. Hong, Y. Shao-Horn, J. M. Tarascon, *Nat. Mater.* **2016**, *15*, 121.
[48] J. Suntivich, H. A. Gasteiger, N. Yabuuchi, H. Nakanishi, J. B. Goodenough, Y. Shao-Horn, *Nat. Chem.* **2011**, *3*, 546.
[49] a) S. Li, J. Zhang, S. Zhang, Q. Liu, H. Cheng, L. Fan, W. Zhang, X. Wang, Q. Wu, Y. Lu, *Nat. Energy* **2024**, *9*, 285; b) H. Shang, X. Zhou, J. Dong, A. Li, X. Zhao, Q. Liu, Y. Lin, J. Pei, Z. Li, Z. Jiang, D. Zhou, L. Zheng, Y. Wang, J. Zhou, Z. Yang, R. Cao, R. Sarangi, T. Sun, X. Yang, X. Zheng, W. Yan, Z. Zhuang, J. Li, W. Chen, D. Wang, J. Zhang, Y. Li, *Nat. Commun.* **2020**, *11*, 3049.
[50] J. Schumann, M. Stamatakis, A. Michaelides, R. Réocreux, *Nat. Chem.* **2024**, *16*, 749.
[51] M. Yu, G. Li, C. Fu, E. Liu, K. Manna, E. Budiyanto, Q. Yang, C. Felser, H. Tüysüz, *Angew. Chem., Int. Ed.* **2021**, *60*, 5800.
[52] J. Liu, H. Liu, H. Chen, X. Du, B. Zhang, Z. Hong, S. Sun, W. Wang, *Adv. Sci.* **2020**, *7*, 1901614.
[53] K. J. Griffith, K. M. Wiaderek, G. Cibin, L. E. Marbella, C. P. Grey, *Nature* **2018**, *559*, 556.
[54] X. Wang, X. J. Gao, L. Qin, C. Wang, L. Song, Y.-N. Zhou, G. Zhu, W. Cao, S. Lin, L. Zhou, K. Wang, H. Zhang, Z. Jin, P. Wang, X. Gao, H. Wei, *Nat. Commun.* **2019**, *10*, 704.
[55] J. Kitchin, J. K. Nørskov, M. Barteau, J. Chen, *J. Chem. Phys.* **2004**, *120*, 10240.
[56] Y. Sun, S. Sun, H. Yang, S. Xi, J. Gracia, Z. J. Xu, *Adv. Mater.* **2020**, *32*, 2003297.
[57] a) D. Reinen, M. Atanasov, S.-L. Lee, *Coord. Chem. Rev.* **1998**, *175*, 91; b) H.-N. Dong, X.-S. Liu, H.-F. Zhou, *Phys. B* **2015**, *477*, 45.
[58] a) K. Jin, H. Seo, T. Hayashi, M. Balamurugan, D. Jeong, Y. K. Go, J. S. Hong, K. H. Cho, H. Kakizaki, N. Bonnet-Mercier, M. G. Kim, S. H. Kim, R. Nakamura, K. T. Nam, *J. Am. Chem. Soc.* **2017**, *139*, 2277; b) J. Kim, Y. Lee, S. Sun, *J. Am. Chem. Soc.* **2010**, *132*, 4996.
[59] in *Electronic and Optical Properties of d-Band Perovskites* (Eds: T. Wolfram, S. Ellialtioglu), Cambridge University Press, Cambridge, **2006**, pp. 199–230.
[60] a) B. Huang, R. R. Rao, S. You, K. Hpone Myint, Y. Song, Y. Wang, W. Ding, L. Giordano, Y. Zhang, T. Wang, S. Muy, Y. Katayama, J. C. Grossman, A. P. Willard, K. Xu, Y. Jiang, Y. Shao-Horn, *JACS Au* **2021**,

1, 1674; b) W. Xu, N. Apodaca, H. Wang, L. Yan, G. Chen, M. Zhou, D. Ding, P. Choudhury, H. Luo, *ACS Catal.* **2019**, *9*, 5074.
[61] Y. Lee, J. Suntivich, K. J. May, E. E. Perry, Y. Shao-Horn, *J. Phys. Chem. Lett.* **2012**, *3*, 399.
[62] a) Q. Ji, L. Bi, J. Zhang, H. Cao, X. S. Zhao, *Energy Environ. Sci.* **2020**, *13*, 1408; b) Y. Wu, J. Cai, Y. Xie, S. Niu, Y. Zang, S. Wu, Y. Liu, Z. Lu, Y. Fang, Y. Guan, X. Zheng, J. Zhu, X. Liu, G. Wang, Y. Qian, *Adv. Mater.* **2020**, *32*, 1904346.
[63] a) K. Mathew, R. Sundararaman, K. Letchworth-Weaver, T. Arias, R. G. Hennig, *J. Chem. Phys.* **2014**, *140*, 084106. b) K. Mathew, V. Kolluru, S. Mula, S. N. Steinmann, R. G. Hennig, *J. Chem. Phys.* **2019**, *151*, 234101.
[64] Y. Sha, T. H. Yu, Y. Liu, B. V. Merinov, W. A. Goddard, *J. Phys. Chem. Lett.* **2010**, *1*, 856.
[65] a) J. K. Nørskov, F. Studt, F. Abild-Pedersen, T. Bligaard, *Fundamental Concepts in Heterogeneous Catalysis*, John Wiley & Sons, Hoboken, **2014**; b) Z. Xue, X. Li, Q. Liu, M. Cai, K. Liu, M. Liu, Z. Ke, X. Liu, G. Li, *Adv. Mater.* **2019**, *31*, 1900430.
[66] a) J. Rossmeisl, A. Logadottir, J. K. Nørskov, *Chem. Phys.* **2005**, *319*, 178; b) E. Skúlason, V. Tripkovic, M. E. Björketun, S. Gudmundsdóttir, G. Karlberg, J. Rossmeisl, T. Bligaard, H. Jónsson, J. K. Nørskov, *J. Phys. Chem. C* **2010**, *114*, 18182.
[67] J. Lu, Y. Zhang, Y. Wen, D. Yu, Y. Chen, K. An, K. Huang, *J. Phys. Chem. C* **2024**, *128*, 17252.
[68] J. Hwang, R. R. Rao, L. Giordano, Y. Katayama, Y. Yu, Y. Shao-Horn, *Science* **2017**, *358*, 751.
[69] F. Ospina-Acevedo, L. A. Albiter, K. O. Bailey, J. F. Godínez-Salomón, C. P. Rhodes, P. B. Balbuena, *ACS Appl. Mater. Interfaces* **2024**, *16*, 16373.
[70] H. Wang, T. Zhai, Y. Wu, T. Zhou, B. Zhou, C. Shang, Z. Guo, *Adv. Sci.* **2023**, 2301706.
[71] a) H. H. Kung, *Transition Metal Oxides: Surface Chemistry and Catalysis*, Elsevier, Amsterdam, Netherlands, **1989**; b) R. Alipour MoghadamEsfahani, S. K. Vankova, E. B. Easton, I. I. Ebralidze, S. Specchia, *Renewable Energy* **2020**, *154*, 913; c) J. Zhao, Y. Xu, S. Liu, X. Ding, *Appl. Surf. Sci.* **2022**, *586*, 152810.
[72] I. Hamada, Y. Morikawa, *J. Phys. Chem. C* **2008**, *112*, 10889.
[73] J. Greeley, T. F. Jaramillo, J. Bonde, I. Chorkendorff, J. K. Nørskov, *Nat. Mater.* **2006**, *5*, 909.
[74] J. Zhang, H. B. Yang, D. Zhou, B. Liu, *Chem. Rev.* **2022**, *122*, 17028.
[75] N.-T. Suen, S.-F. Hung, Q. Quan, N. Zhang, Y.-J. Xu, H. M. Chen, *Chem. Soc. Rev.* **2017**, *46*, 337.
[76] G. Kresse, J. Furthmüller, *Phys. Rev. B* **1996**, *54*, 11169.
[77] P. E. Blöchl, *Phys. Rev. B* **1994**, *50*, 17953.
[78] J. P. Perdew, K. Burke, M. Ernzerhof, *Phys. Rev. Lett.* **1996**, *77*, 3865.
[79] J. K. Nørskov, J. Rossmeisl, A. Logadottir, L. Lindqvist, J. R. Kitchin, T. Bligaard, H. Jonsson, *J. Phys. Chem. B* **2004**, *108*, 17886.